

Tectonics

RESEARCH ARTICLE

10.1029/2019TC006046

Key Points:

- Large-scale obliquity in the northern MER increases toward Afar with transtensional kinematics
- The Boset magmatic segment is characterized by two main NNE orientated fault zones, bounding a nested graben
- Maximum slip rates are ~0.37 mm/year in ~300 Ka volcanic deposits and ~4.3 mm/year offsetting ~6 Ka lavas of Boset

Supporting Information:

- Supporting Information S1

Correspondence to:

M. Siegburg,
melanie@siegburg-shs.de

Citation:

Siegburg, M., Bull, J. M., Nixon, C. W., Keir, D., Gernon, T. M., Corti, G., et al. (2020). Quantitative constraints on faulting and fault slip rates in the northern Main Ethiopian Rift. *Tectonics*, 39, e2019TC006046. <https://doi.org/10.1029/2019TC006046>


Received 23 DEC 2019

Accepted 6 JUL 2020

Accepted article online 9 JUL 2020

© Wiley Periodicals LLC. The Authors. This is an open access article under the terms of the Creative Commons Attribution License, which permits use, distribution and reproduction in any medium, provided the original work is properly cited.

Quantitative Constraints on Faulting and Fault Slip Rates in the Northern Main Ethiopian Rift

Melanie Siegburg¹ , Jonathan M. Bull¹ , Casey W. Nixon² , Derek Keir^{1,3} , Thomas M. Gernon¹ , Giacomo Corti⁴ , Bekele Abebe⁵, David J. Sanderson¹ , and Atalay Ayele⁶

¹School of Ocean and Earth Science, National Oceanography Centre Southampton, University of Southampton, Southampton, UK, ²Department of Earth Science, University of Bergen, Bergen, Norway, ³Dipartimento di Scienze della Terra, Università degli Studi di Firenze, Florence, Italy, ⁴Consiglio Nazionale delle Ricerche, Istituto di Geoscienze e Georisorse, Florence, Italy, ⁵Department of Earth Sciences, Addis Ababa University, Addis Ababa, Ethiopia, ⁶Institute of Geophysics, Space Sciences, and Astronomy, Addis Ababa University, Addis Ababa, Ethiopia

Abstract The Boset magmatic segment (BMS) of the northern Main Ethiopian Rift (MER) is an ideal natural laboratory to investigate the kinematics, interaction, and rates of activity within a fault network in a magma-rich rift. In this paper we take advantage of the availability of (1) high-resolution remote sensing data (LiDAR, ASTER); (2) absolute age chronology on offset reference surfaces; and (3) well-exposed active normal fault arrays to place new constraints on rift kinematics and strain distribution, and to quantify the architecture and fault slip rates at different temporal scales within a magmatic segment. We found that the rift border faults strike approximately NE, while the younger faults in the rift segments strike NNE. Analyses of geometric rift parameters show that the axial active part of the rift is transtensional with an increase of the shear component northward. The fault displacement analyses and displacement:length ratios increase toward the segment tips, suggesting a significant contribution of fault growth by linkage. In contrast, magmatism is focused on the segment center and localized to a narrow zone. Estimated fault slip rates vary, with rates of up to ~0.37 mm/year in ~0.3 Ma old rift floor deposits, whereas higher rates of up to ~4.4 mm/year are observed for faults cutting through ~6 Ka lavas. The difference in slip rates indicates short-term variability or a very active recent episode compared to long-term low average slip rates.

1. Introduction

A quantitative understanding of fault networks and their kinematics including growth, reactivation, and interaction in magma-assisted continental rifts has been hampered by a lack of chronological constraints, but studies worldwide provide a qualitative framework. In this paper we build on previous studies from Iceland (e.g., Bull et al., 2003; Grant & Kattenhorn, 2004; Tentler, 2005; Villemin & Bergerat, 2013); Hawaii (e.g., Bubeck et al., 2018; Holland et al., 2006; Kaven & Martel, 2007; Martel & Langley, 2006); the Taupo Rift Zone, New Zealand (e.g., Rowland et al., 2010; Rowland & Sibson, 2001, 2004); and the East African Rift (EAR) (Acocella et al., 2011; Casey et al., 2006; Corti, 2009; Rowland et al., 2007) by characterizing the structural style of the active Boset magmatic segment (BMS) of the northern Main Ethiopian Rift (MER). Here, previous work has provided a relative and absolute chronological framework (Abebe, Manetti, et al., 2005; Chernet et al., 1998; Siegburg et al., 2018). Thus, we aim to investigate the faulting history within a magmatic segment of a tectonically active magma-rich rift.

Since the Quaternary, extension in the northern MER is thought to have been mainly focused on ~20-km-wide, ~70-km-long magmatic segments characterized by a dense fault distribution, aligned with young cones and fissures, and cutting young lava flows (Ebinger & Casey, 2001) (Figure 1). Previous studies have mainly focused on characterizing large rift-scale distribution of faults and their spatial relationship to volcanism (e.g., Abebe, Coltorti, & Pizzi, 2005; Agostini et al., 2011; Casey et al., 2006; Corti, 2009; Corti, Sani, et al., 2013; Ebinger & Casey, 2001; Wolfenden et al., 2004), with few placing quantitative constraints on fault displacement, geometries, and slip rates (Abebe, Manetti, et al., 2005; Casey et al., 2006; Kurz et al., 2007; Pizzi et al., 2006; Williams et al., 2004).

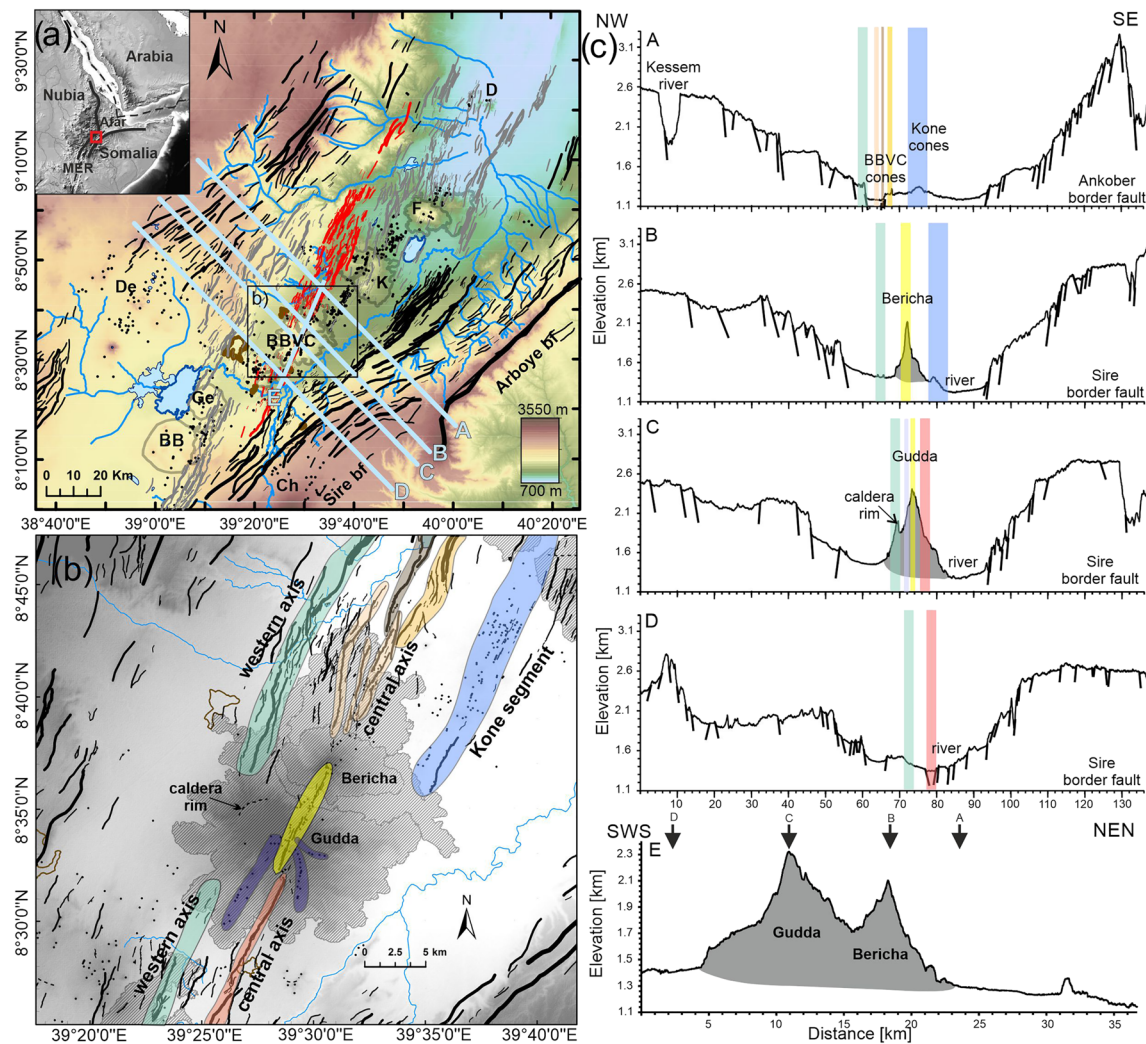


Figure 1. Topography of the Boset-Bericha Volcanic Complex (BBVC) and main tectonic and volcanic elements. (a) Topography and main fault-fracture (line thickness weighted according to fault length) set with border faults (black), distribution of cones and craters (small, black dots), magmatic segment faults (Wonji faults, gray), and BMS faults (red). Cross-section locations are indicated (blue, A–E). Other volcanic edifices are labeled Bora-Bericha (BB), Gedemsa (Ge), Kone (K), Fantale (F), and Dofan (D). (b) The main volcano-tectonic elements represent the western axis (green), central axis (warm colors), and exposed remnant caldera rim from the central part of the BMS. Aligned cones and craters (blue-violet) are distributed on the central axis and Kone segment. (c) Four representatives across-rift topographic profiles (A–D) and one along-axis profile (E) derived from ASTER data (resolution 30 m). Colored bands show the position of volcano-tectonic features identified in (b).

In order to understand the structural morphology and architecture along a single segment, we focus on the BMS, located between the Gedemsa and Kone segments in the northern MER (Figures 1 and 2). The BMS is 70–90 km long, oriented NNE–SSW, and includes Quaternary–Recent volcanic rock and pyroclastic deposits (Abebe, Manetti, et al., 2005). The BMS is a perfect natural laboratory to quantitatively constrain faulting and slip rates, due to (1) the availability of detailed mapped lava units with a relative and absolute chronology (Siegburg et al., 2018); (2) recent tectonic and magmatic activity (i.e., Fontijn et al., 2018; Siegburg et al., 2018; Wadge et al., 2016); (3) and high-resolution remote sensing data (LiDAR, ASTER, and SRTM). In this paper, the fault network on several magmatic segments between Gedemsa and Dofan volcanoes in the northern MER is characterized in terms of its overall rift geometry. In addition, fault kinematics, fault distribution, and the spatial variability of fault slip are analyzed within the BMS in order to characterize the structural style of an active magmatic segment. We then also use these data along with lava flow ages to place quantitative constraints on fault slip rates and the importance of faulting to the overall extension.

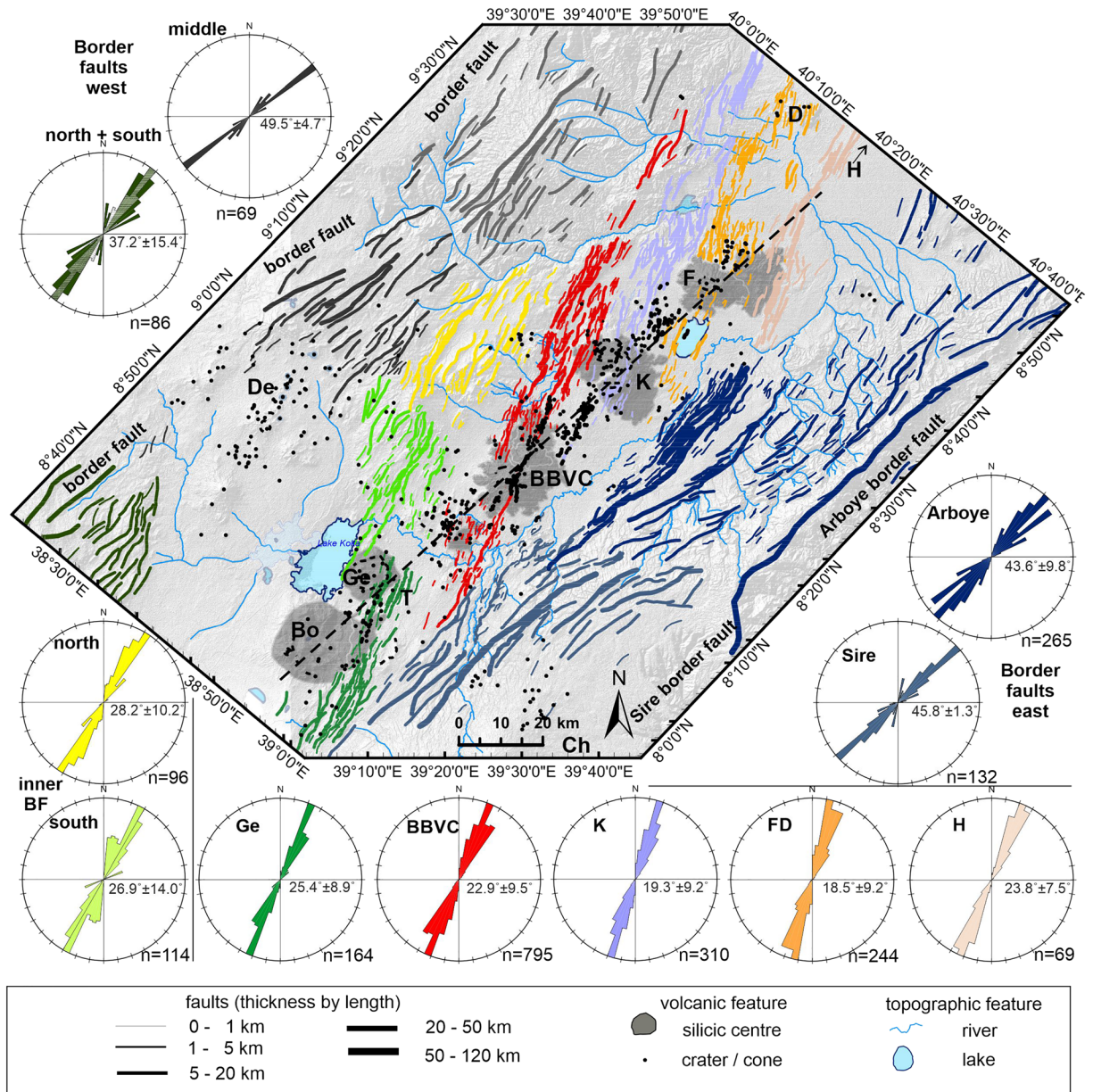


Figure 2. Map and length-weighted rose diagrams showing the orientation of faults for different rift segments and border faults (Sire, Arboye, and western border faults) around the BBVC in the northern MER (Figure 1). The main volcanic centers (gray), cones, and craters (black dots) and significant rivers and lakes (light blue) are shown on the map. Volcano-tectonic segments on the map are linked to rose diagrams by color and label, Bora-Bericha (Bo), Gedemsa (Ge), Boset-Bericha Volcanic Complex (BBVC), Kone (K), Fantale-Dofan (FD), and Hertali (H). Aligned volcanic edifices on the border faults are Debre Zeit (De) and Chilalo (Ch). Border faults are intersected by rivers and erosion canyons at the rift margin, and border fault orientation is more variable on the western compared to the eastern margin.

2. Geological Background

The MER (Figure 1) is in the northern sector of the EAR and separates the Somalian plateau (Somalian plate) and Ethiopian plateau (Nubian plate) (e.g., Bilham et al., 1999; Birhanu et al., 2016) (Figure 1). Extension in the northern MER is thought to have started at ~11 Ma and was associated with volcanism on NE striking border faults (e.g., Arboye, Sire and Ankober border faults) with vertical offsets of several hundred meters (Chernet et al., 1998; Rooney et al., 2014; WoldeGabriel et al., 1990; Wolfenden et al., 2004) (Figures 1 and 2).

Through time (since 2 Ma), extension and volcanism have become focused on the central part of the ~60- to 100 km-wide graben (Hayward & Ebinger, 1996), resulting in ~20-km-wide, right-stepping en echelon

magmatic segments (Casey et al., 2006; Corti, 2009; Ebinger & Casey, 2001; Keir et al., 2006; Mohr, 1962, 1967), also known as the Wonji fault belt (WFB) (Mohr, 1962) (Figures 1 and 2). These segments are dominated by closely spaced NNE striking small offset faults and fissures, aligned monogenetic cones, and Quaternary-Recent silicic volcanoes (Ebinger & Casey, 2001; Kurz et al., 2007). They range 40–70 km in length and are mainly oblique (NNE) to the rift margin orientation (NE). Segment spacing is variable, with lateral segment offsets ranging from ~2 km (BMS-Kone) to ~18 km (Gedemsa-BMS). Some authors interpret the segment tips to be overlapping and accommodating strain transfer but without the development of transfer faults (Casey et al., 2006). The Quaternary-Recent faults in the magmatic segments are commonly spatially associated with volcanic centers and aligned cones (e.g., Ebinger & Casey, 2001). As a result, there has been a debate regarding whether fault growth is dike driven (e.g., Casey et al., 2006; Ebinger & Casey, 2001) or purely of tectonic origin (e.g., Acocella et al., 2002; Corti, 2008).

GPS measurements and plate kinematic modeling suggest that the MER extends at ~5 mm/year in the ESE direction (e.g., Bendick et al., 2006; Birhanu et al., 2016). Approximately ~2 mm/year of extension occurs within the rift valley (Birhanu et al., 2016), with the locus of seismicity, young faults, and lava flows, suggesting the majority of the rift valley extension is mainly focused on the magmatic segments (Ebinger & Casey, 2001; Keir et al., 2006). Plate kinematic models indicate that the motion between the Nubian and Somalian plates has occurred since at least 16 Ma and has likely been stable (DeMets & Merkouriev, 2016).

Geophysical studies suggest a high density of mafic intrusions beneath the magmatic segments, including the BMS (Cornwell et al., 2006; Mackenzie et al., 2005; Whaler & Hautot, 2006) with surface morphology, suggesting a focus of magmatism in the segment center (Kurz et al., 2007). The BMS contains NNE trending faults cutting through the Quaternary-Recent Boset-Bericha Volcanic Complex (BBVC) in the segment center and terminating to the north and south at the western and eastern rift margins, respectively (Figures 1a and 2). The BBVC is one of the largest stratovolcanic complexes (17 km E-W and 20 km N-S) in the northern MER and comprises the northern Bericha Volcano (2,120 m) and the southern Gudda Volcano (2,447 m) (Figure 1b). For both volcanoes, episodic activity at the volcanic center is recorded for the last ~16 Ka (Sieburg et al., 2018), with recent activity on the central fissure between the edifices (Fontijn et al., 2018; Sieburg et al., 2018).

3. Data and Methodology

3.1. Remote Sensing Data and Spatial Analysis

We mapped tectonic and volcanic features at, and around, the BBVC in ArcGIS using high-resolution Light Detection and Ranging (LiDAR) elevation data combined with more regional Advanced Spaceborne Thermal Emission and Reflection Radiometer (ASTER) data, Shuttle Radar Topography Mission (SRTM) data, and field observations (Figure 2). The high-resolution LiDAR data were collected during a NERC ARSF LiDAR survey over the BBVC in November 2012 and have 2-m horizontal and 0.2-m vertical resolution (Figure S1). Field work was used to ground-truth volcanic features and fault displacement observed in the remote sensing data. The remote sensing data were imported into ArcGIS in which faults, fissures, craters, and cones were interpreted and digitized. To aid interpretation, slope, aspect, and hillshade functions were applied to LiDAR and ASTER data to identify gradients, dip directions, and degree of erosion, respectively. The density of craters and cones is determined by the kernel density tool in ArcGIS, using contour plots gridded at 100 m with a search radius of 500 m for point sources.

3.2. Fault Geometry and Displacement Measurement

The remote sensing data reveal the overall topography and well-exposed fault scarps and fissures that offset and deform lava flows and pyroclastic deposits. Analysis of remote sensing data can only quantify the brittle component of strain after the time of emplacement of the displaced lava. Intrusive strain, which is estimated at >50% from the minimum volume of intrusive material (e.g., Ebinger et al., 2017; Keir et al., 2006), is not captured in these analyses. Regional topography and strain distribution over the rift valley were derived from Aster data. In total, over 2,300 fault traces were digitized and analyzed in terms of their orientation, using length-weighted rose diagrams and maps as well as displacement data. Elevation values of hanging wall and footwall surfaces (from the LiDAR and ASTER data) were used to measure throw or vertical separation every 100–200 m along faults within the BMS (Figure S1 in the supporting information). As the faults form steep dipping fault planes based on field observations and spatial analyses, the measured throws and scarp

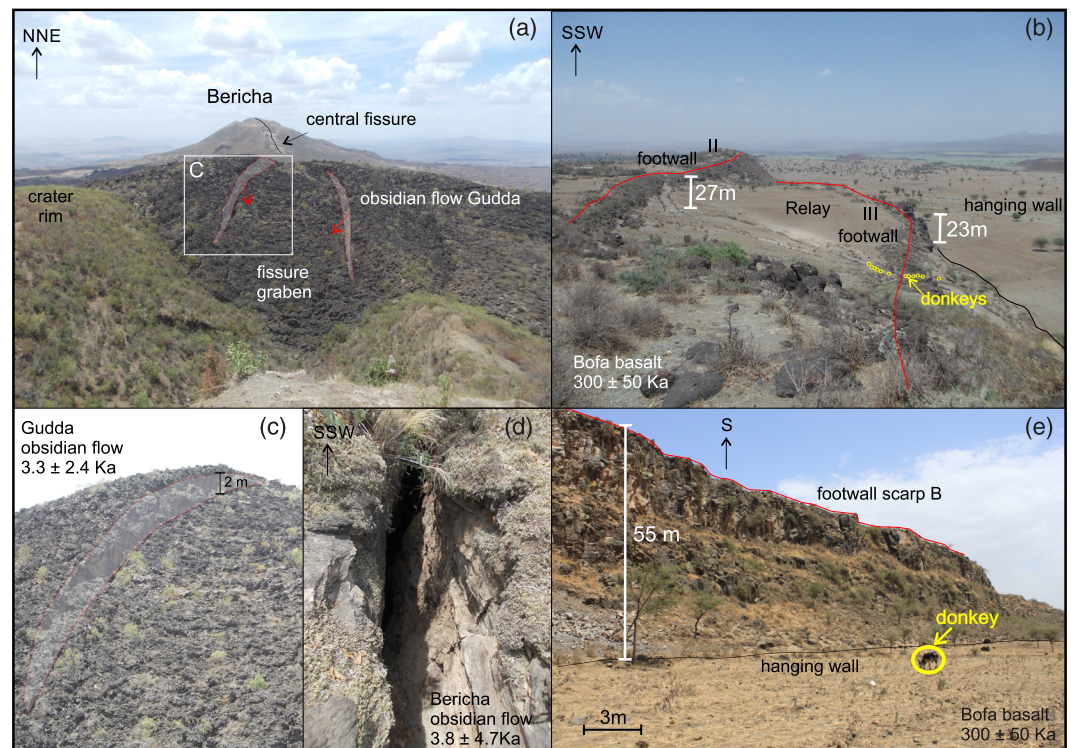


Figure 3. Photographs indicating some key magmatic and structural features at the Boset magmatic segment. (a) View from Gudda crater wall toward NE on the obsidian lava flow cut by fissure with marked faults and zoom in on the western fault in (c). (b) Relay ramp (within LiDAR data) on the southern fault in the Bofa basalt between Faults II and III, looking along fault scarp toward the SW. (a) A crack in Berichas lava flow along the central axis with 1- to 2-m opening. (e) Fault scarp in the Bofa basalt close to relay ramp between fault (b) and (c). For scale donkeys are marked as yellow circles in (b) and (e). The position of the photographs is shown in Figure 6.

heights were used to approximate their displacements and minimum displacements, respectively. Based on the vertical resolution of the data sets, measurements are considered to have errors of ± 10 m and ± 0.4 m for the ASTER and LiDAR data, respectively. More detailed displacement profiles were produced for selected faults, with measurements taken at intervals down to 25 m within the LiDAR data, to characterize spatial variations in displacement at locations of fault interaction and linkage. Fault linkage zones (e.g., relay ramps) were investigated by along and across ramp profiles to determine their size, orientation, and slopes.

3.3. Age Constraints for Slip Rate Calculations

Minimum average slip rates were calculated on the basis of fault displacement analyses combined with relative and absolute age constraints from the surrounding chronostratigraphy (e.g., Siegburg et al., 2018; Table S1). The BMS (Figures 1 and 2), defined above, is emplaced, at its north and south parts through per-alkaline tuff, ash flow, and ignimbrites of the Miocene Nazret pyroclastic group (5.2 to 2.5 Ma, Abebe, Manetti, et al., 2005) (Table S1). NE of the BBVC edifice, lacustrine sediments cover the rift floor. The central part of the segment is covered by Quaternary volcanic silicic lava flows of the BBVC (Siegburg et al., 2018) and Pleistocene to Holocene Wonji mafic rift floor basalts between the BBVC and the Kone edifice as well as the Pliocene to Pleistocene Bofa basalt (300 ± 50 Ka; Chernet et al., 1998) south of the BBVC edifice (Figures 2 and 3). Some parts of the Bofa basalt unit south of the BBVC are covered by the Chefe Donsa pumice (Figure 3).

4. MER Structure and Topography Around the BMS

The rift topography is variable in the northern MER with the rift widening and decreasing in elevation northward Afar (Figures 1), best illustrated by simple topographic profiles: four NW to SE across-rift (A–D) and one SSW–NNE along-rift axis profile (E) (Figure 1). For most across-rift profiles, there is a marked

asymmetry with a steeper eastern rift margin (Figure 1, Profiles A–D). In Profiles C and D (Figure 1), the NW rift margin is characterized by two topographic steps down from the ~2,600-m-high Ethiopian plateau to the rift valley floor. The SE rift margin topography decreases from the Arboye border fault ridge (~3,260 m) in the north to the Sire border fault plateau (~2,680 to 2,860 m; Figure 1) in the south with a curving Arboye fault trend at the transition of the border fault systems. The rift floor is ~30 km wide with elevation changing from ~1,450 m in the SW to 900 m in the NE and slightly increasing elevation toward the volcanic edifice (Figure 1, Profile E), with the summit of Gudda rising 2,447 m above the rift floor.

At the BBVC, the eastern rift floor is less elevated than the western rift floor (Figure 1, Profiles B–D), whereas to the north of the BBVC the rift floor is offset by a graben and cone line, resulting in a less tilted rift floor geometry (Figure 1, Profile A). Rivers drain northward on the rift margins producing large canyons parallel to border faults and downslope toward the rift center, where they follow the tilted rift floor and drain along the eastern border fault (Figures 1a and 2).

5. Characterization of the Regional Fault Population

5.1. Orientation

Extension is characterized by normal faults, with fractures and fissures at the magmatic segments. The orientation of the western margin border faults (average strike of ~N037°E) range between ~N030°E in the north and ~N050°E northwest of the BBVC edifice (top left in Figure 2; Table S2). The fault system in between the border faults and the rift axis (bottom left in Figure 2; Table S2) has an orientation intermediate between the two, with the change in orientation coincident with a change to a two-step geomorphology in topography (Figure 1, Profiles B–D).

Border faults on the eastern rift margin are more pronounced than on the western rift margin, with orientations of $N043.6^\circ E \pm 9.8^\circ$ for the northern (Arboye) and $N045.8^\circ E \pm 1.3^\circ$ for the southern border faults (Sire) (Figure 2). Fault orientations in the central rift are divided into different magmatic segments, defined by fault density, distribution, orientation, and alignment with central silicic volcanic complex. The BMS is defined by faults aligned with the BBVC. Their length weighted average strike decreases from ~N025°E to N018°E northward (Figure 2; Table S2). The orientation of aligned craters and cones was calculated by fitting a best fit line to adjacent 3 to 20 features (Figure 1b; Table S2). Cones and craters subparallel to the magmatic segments have more easterly strikes compared to fault averages (Table S2). We also observed radial cone lines on the southeastern slope of Gudda (~N004°E) and northeastern slope of Bericha (~N051°E). Some WSW-ENE to W-E aligned craters and cones (~N077°E to N087°E) are present on top of Gudda edifice and south of Kone and mark the rim of old calderas (Cole, 1969; Siegburg et al., 2018). Nonrift parallel cone fields are also present between magmatic segments (Figure 1b).

Based on the orientations of individual magmatic rift segments (F) and the overall rift trend (P) of $N048^\circ E \pm 005^\circ$ (alignment of volcanic centers; Figure 2) relative to the recent plate motion vector (V), we classified the rift geometry in a kinematic analyses in terms of transtensional, oblique, or orthogonal opening following the model of Sanderson and Marchini (1984) and approach of Tuckwell et al. (1996) (Figure 4). This model uses the relation of α and ϕ , which describes the angular relationships between V to P and to F , respectively (Figure 4; Table S2). For the current overall geometry, we calculated the plate motion vector ($V_{\text{calculated}}$) based on the graphical construction of McCoss (1986), by using the observed length-weighted fault average orientations for maximum horizontal stress ($S_{\text{Hmax}} = \sigma_2$) and their perpendicular angle for minimum horizontal stress ($S_{\text{Hmin}} = \sigma_3$) (Table S2). Here, the calculated plate motion vector ($V_{\text{calculated}}$) is independent of the plate velocity. The calculated plate motion vectors ($V_{\text{calculated}}$) progressively increase southward from N079°E at Fantale segment to N093°E at Gedemsa segment. Using $V_{\text{calculated}}$ for each segment, all segments are transtensional with α of 31 to $45 \pm 10^\circ$ and ϕ 60.5 to $67.5 \pm 14^\circ$ (Figures 2 and 4; Table S2).

The $V_{\text{calculated}}$ values are lower than other observed indicators of plate motion (V_{observed} of $095 \pm 009^\circ$ and $103 \pm 010^\circ$), such as from GPS measurements (Bendick et al., 2006; Birhanu et al., 2016), the elliptical shapes of calderas (Casey et al., 2006), fault movement indicators (Acocella & Korme, 2002; Pizzi et al., 2006), and earthquake focal mechanisms (Keir et al., 2006; Muluneh et al., 2018).

Using V_{observed} of 095° , the current rift geometry resulted in a transtensional model ($\phi < 90^\circ$, $F \neq P$) with α of $47 \pm 14^\circ$ and ϕ of 67 to $76 \pm 19^\circ$. A V_{observed} of 103° generates an α of $55 \pm 15^\circ$ and ϕ of 75 to $84 \pm 20^\circ$ and can

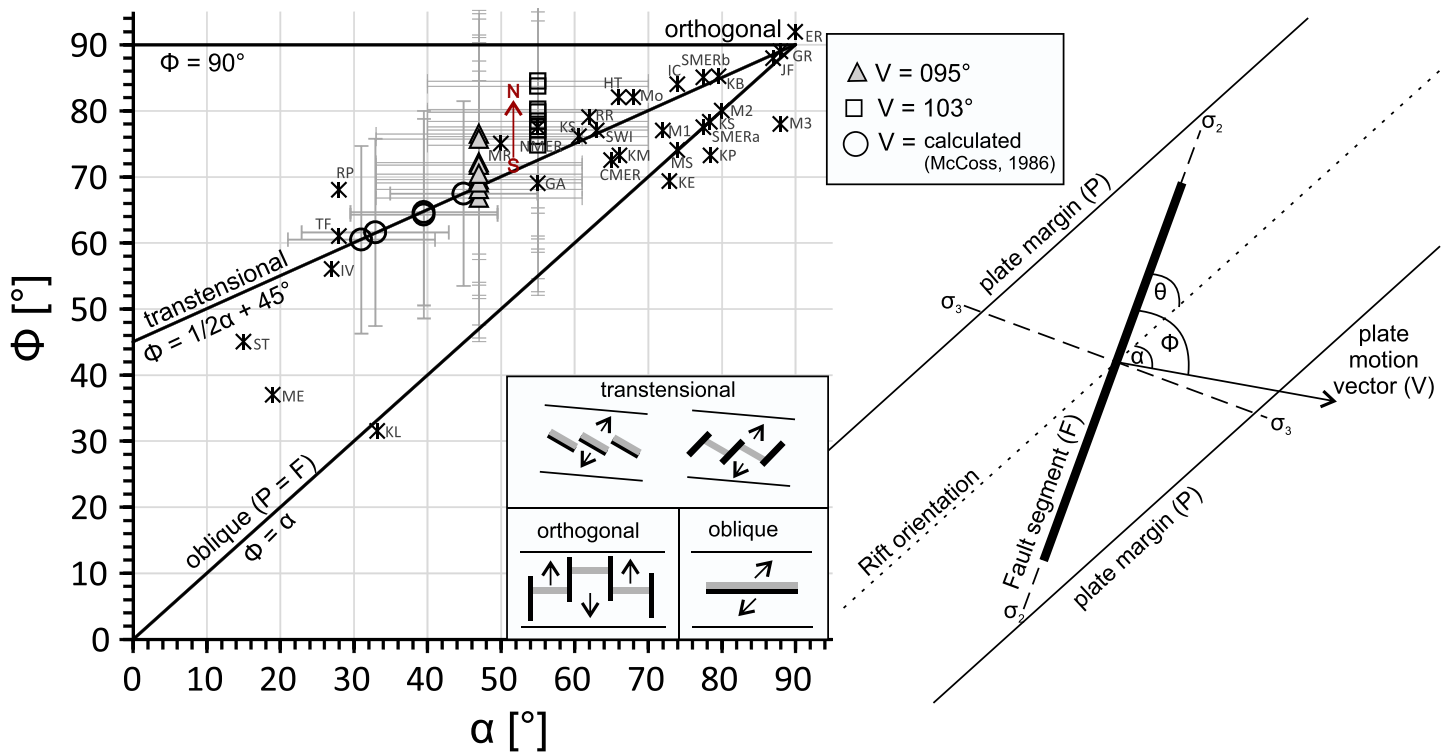


Figure 4. Rift geometry of the northern MER. Three alternative rift geometries—orthogonal, transtensional, and oblique after Tuckwell et al. (1996). Φ and α are defined by the angular relationship between the overall rift orientation (P), fault segment trend (F), and the plate motion vector (V). Data points with error bars are from individual segments of the northern MER shown in Figure 2 and suggest a transtensional geometry. Plate motion vectors are calculated after McCoss (1986) for transtensional kinematics (circle), ranging between 079° and 093° between Fantale (NE) to Gedemsa (SW), as shown by the red arrow. The two fixed plate motion vectors of $N095^\circ \pm 009^\circ$ (triangle) and $N103^\circ \pm 010^\circ$ (square) are from GPS measurements (Bendick et al., 2006; Birhanu et al., 2016), plate tectonic models (Chu & Gordon, 1999; Jestin et al., 1994), elliptical shape of calderas (Casey et al., 2006), fault movement indicators (Acocella & Korme, 2002; Pizzi et al., 2006), and earthquake focal mechanisms (Keir et al., 2006; Muluneh et al., 2018) of the MER. Other rifts and spreading centers (cross) are added for comparison: MAR (M1-3); Reykjanes Ridge (RR); Reykjanes Peninsular (RP); NE Iceland (IC); Tjornes fracture zone (TF); Mohn's Ridge (MR); SW Indian Ridge (SWI); Gulf of Aden (GA); East Pacific Ridge (EPR); Juan de Fuca Ridge (JF); Galapagos Ridge (GR); Ecuador Rift (ER); Imperial Valley (IV); Manus Spreading Center (MS); Manus ETZ (ME); Siqueiros Transform (ST) (Tuckwell et al., 1996); Kenya The Barrier (KB); Kenya Emurungolok (KE); Kenya Silali (KS); Kenya Paka (KP); Kenya Menengai (KM); Kenya Longonot (KL); Kenya Suswa (KS) (Robertson et al., 2015), northern, central, and southern MER (NMER, CMER, SMERa, and SMERb) (Agostini et al., 2011); Monowai (Mo); and Havre trough (HT) (Wormald et al., 2012).

be characterized mainly as transtensional opening, with a trend from south to north toward the short segment oblique opening model ($\phi = 90^\circ$, $F \neq P$), without obvious transform faults. The ranges of ϕ reflect different orientations of fault segments with higher ϕ for the northern segments (Figures 2 and 4; Table S2), further described in section 8.1.

5.2. Strain Distribution

Variation in tectonic deformation in the study area was determined by cumulative profiles of vertical surface separations across faults, and fault frequency along the cross-rift sections (Figure 1). The rift-wide fault distribution (Figure 5) was analyzed using the method developed by Putz-Perrier and Sanderson (2008a, 2008b), where the cumulative distribution of faults is compared with a uniform distribution (Figure 5, dashed line D_{uni}). The degree to which maximum deviation is above (D^+) and below (D^-) the uniform line (Figure 5, dotted line) can be used as a measure of fault heterogeneity V' by using the absolute sum of both ($V' = [D^+] + [D^-]$). Cumulative throws for each profile are normalized to 1 to allow comparison between different profiles. This method results in V' values ranging between 0 and 1, with 0 representing a homogeneous distribution.

The cross-rift sections (Figures 1 and 5) each include between 133 and 146 picked fault scarps with a cumulative vertical scarp height of up to 6.05 km for the total rift, measured with 30 m resolution ASTER data. Both fracture frequency and separation show larger deviations from a uniform line at the rift margins and

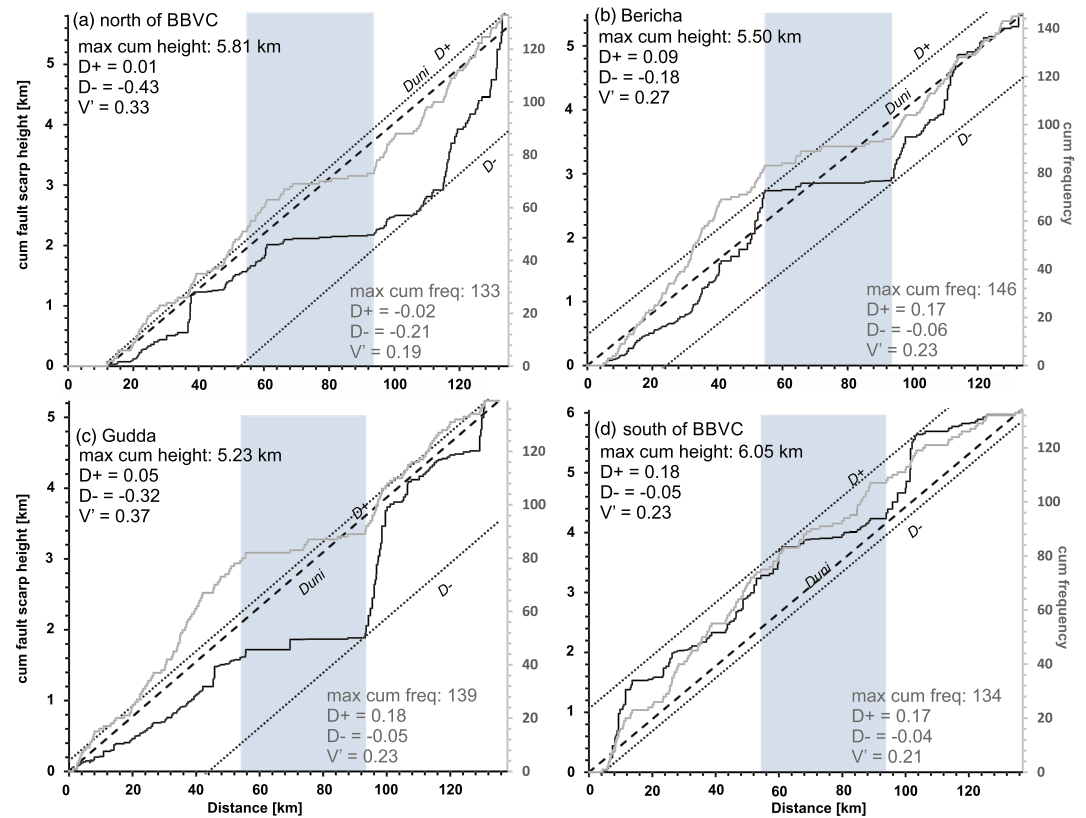


Figure 5. Strain distribution of cumulative vertical surface separation (black) and fault frequency (gray) along the four cross-ribs sections (a) north of the BBVC, (b) on top of the Bericha, (c) on top of the Gudda, and (d) south of the BBVC. The location of the four cross-ribs sections are shown in Figure 1. The rift graben is marked in blue-gray. D^+ and D^- (dotted line) are the maximum deviation from a uniform distribution line (dashed), here shown as an example for the cumulative vertical fault separation. V' represents the absolute sum of D^+ and D^- , given as an indicator for homogenous distribution (~ 0) and heterogeneous distribution (> 0), independent of the start value (Putz-Perrier & Sanderson, 2008b). All values are given as normalized values to the maximum. Note that the cross-ribs section north of the BBVC (a) starts around 12 km (see plot a) due to the canyon of the Kessem river, which is not considered here.

a plateau in the rift center (Figure 5). The heterogeneity of fault frequency is very similar for the four cross-ribs sections with V' varying between 0.19 and 0.23. Steeper slopes (larger deviation above uniform line [$D^+ > D^-$]) indicate higher fault intensities and locations at the border system of the western rift margin (Figures 5a–5c). Cumulative vertical separations of faults are less heterogeneous in the southern BBVC and Bericha cross-ribs section with a V' of 0.23 and 0.27, respectively (Figures 5b and 5d), and most homogeneous in the northern BBVC (V' of 0.33) and Gudda (V' of 0.37) cross-ribs sections (Figures 5a and 5b). Fault separations show larger deviations below the uniform line ($D^- > D^+$), suggesting larger fault offsets at the eastern border fault system (Figures 5a–5c).

5.3. Fault Distribution and Cone Density

Maps of faults and volcanic cones around the BMS show the distribution and frequency of tectonic features and density of volcanic features (Figure 6). The BMS comprises two main NNE-SSW oriented fault zones of closely spaced faults (50- to 500-m space) with mainly vertical displacement, together forming a graben north and south of the BBVC edifice. The graben width of ~ 5 km is similar in scale to the alignment of the BBVC caldera (Figures 1 and 6). The western BMS fault zone is mainly exposed north and south of the BBVC as a normal fault with a dominant ESE dip direction. The central fault zone is exposed along the whole segment as a range of normal faults dipping toward the WNW south of the BBVC, but also as a fissure and cone-crater chain at, and north of, the edifice (Figures 1 and 6). It is characterized by several parallel subsegments dominated by either faulting or fissuring (Figure 1).

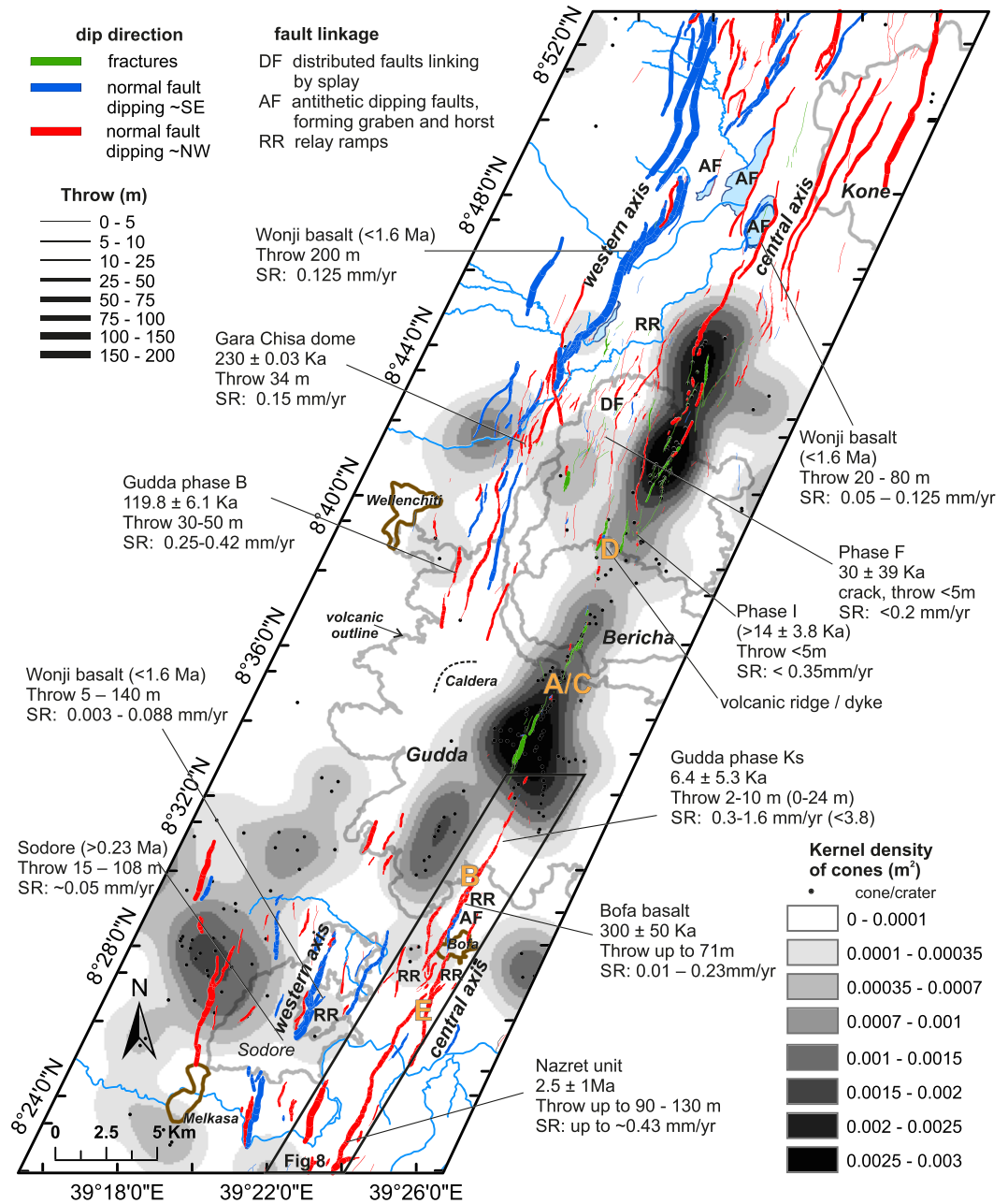


Figure 6. Map illustrating throw variation (represented by line thickness) for the main faults and fissures in the central BMS region. Colors of faults indicate dip direction and type. The volcanic edifice is shown in the background. The exposed caldera rim is marked. The eastern part of the caldera rim is covered by younger volcanics. Cone and crater distribution (black dots) and density, illustrated by the gray shaded contours, represent the location of volcanism. The density contour plots are gridded at 100 m with a search radius of 500 m, with the dark shading indicating high-density areas. The black box south of the Gudda edifice shows the extent of Figure 8. Capital letters indicate the position of field photos of Figure 3. The type of fault linkage is indicated and presented in more detail in Figure 10.

High cone and crater frequency and density around the BMS are focused and aligned on the central fault zone at, and north, of the BBVC edifice, and along the Kone segment (Figures 1, 2, and 6). Beside cone and crater alignments, rhyolitic volcanic ridges (north of the Bericha) and fissures sourcing lava flows (Figures 1 and 6) are present and are indicative of dike intrusions. Cone and crater density between the BMS and Gedemsa segment are less dense but aligned suborthogonal to fault segments (Figures 2 and 6).

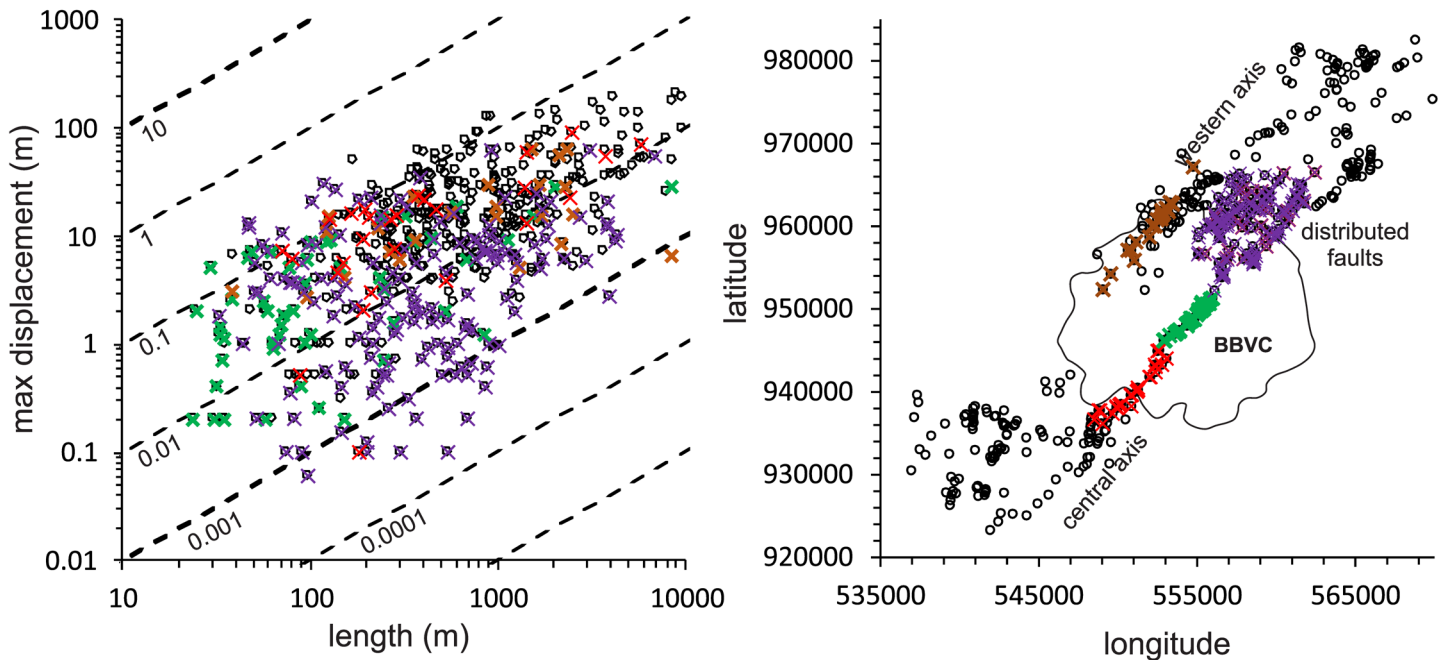


Figure 7. Maximum displacement versus length of faults along the BMS showing a spatial dependence along the segment using LiDAR (color cross) and Aster (black circle) data. LiDAR data along the BMS are color-coded in southern central axis (red), edifice central axis (green), distributed faults north of the BBVC (violet), and western axis (brown).

6. Fault Interaction and Kinematics

6.1. General Fault Characteristics Along the BMS

Fault sizes determined from LiDAR and ASTER imagery along the BMS cover several orders of magnitude, with measured lengths and throws ranging from 10 to 15 km and <1 to 200 m, respectively (i.e., Figure 7).

Measured fault throws are largest north and south of the BBVC along the western and central fault zones, while between them, and over the volcanic center, faults are smaller (throw <5 m) and associated with more opening. They appear to have acted as conduits for fissural eruption of lava on top of the edifice (Figure 6). The largest fault, with a maximum throw of ~200 m, is exposed on the western fault zone between the BBVC and Kone volcano (Figure 6). Throws decrease to the south and are distributed onto numerous smaller faults with throws of 30–50 m northwest of Gudda and Bericha. In the southwest of the BBVC, throws along the western fault zone increase again up to ~140 m (Figure 6). The central fault zone (Figure 6) has the largest throws to the north (20–80 m) on northwest dipping faults. The maximum throws in the south of the BBVC are around ~60 m in the Bofa basalt and up to 120 m in Nazret unit (Figures 6 and 8). In the next section the southern part of the central fault zone is explored in more detail (box in Figure 6).

The relationship between maximum throw and length in Figure 7 follows a power-law trend, that has been documented for many normal fault populations (e.g., Bailey et al., 2005), with the majority of the faults occurring between throw:length ratio contours 0.001 and 0.1. However, grouping the data spatially highlights local variations in throw:length ratios along the BMS (Figure 7).

The distributed faults and the faults on the central axes at the volcanic edifice (purple and green crosses, respectively) appear to exhibit a broader range of maximum throws with a majority of faults exhibiting lower throw:length ratios (0.001–0.01). In contrast, the southern central axis and western axis faults (red and brown crosses, respectively) generally have greater maximum throws producing an overall higher throw:length ratio (0.01–0.1). This variation does not appear to be biased by the resolution of data (LiDAR and ASTER) and instead correlated with proximity to the volcanic complex.

Throughout the fault network of the BMS, we observe an interaction between the two fault zones (central and western axis) and between individual faults by linkage, relay ramps, and splayed faults, suggesting

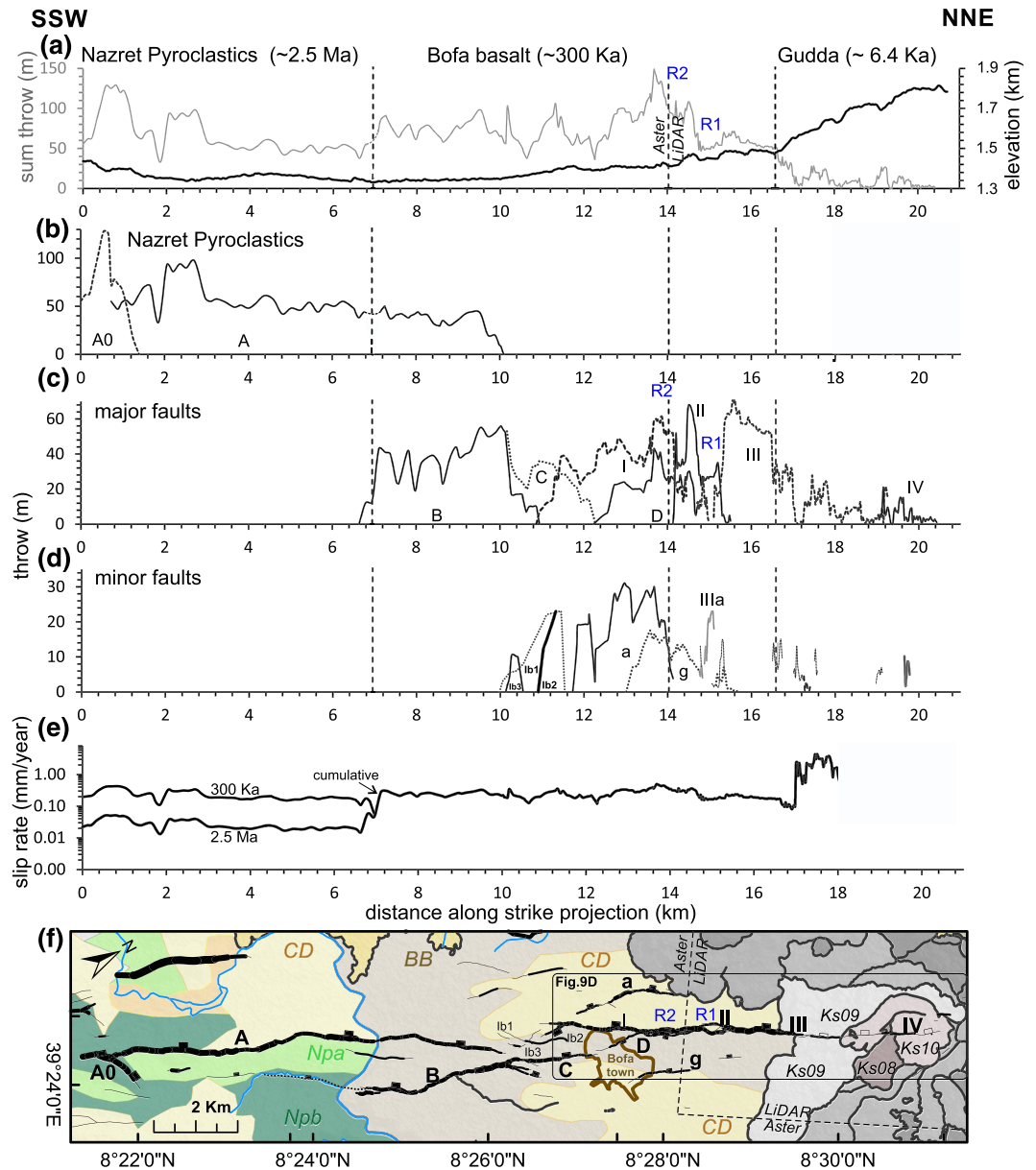


Figure 8. Analysis of a normal fault linked by relays of different scales south of the BBVC. (a) Cumulative throw along the normal fault system; (b) throw on Nazret pyroclastics (Np); (c) major faults in the Bofa basalt unit (BB) and Gudda lavas; (d) minor faults in the Bofa basalt unit (BB) and Gudda lavas; (e) slip rate variation along the normal fault system with slip rate of cumulative throw; slip rates for the Nazret unit is calculated assuming ages of 2.5 Ma and 300 Ka; (f) map of faults and offset geological units: Nazret pyroclastics associated with felsic domes and lavas (Npa), and welded pyroclastic flows (Npb), the Bofa basalt (BB), and Chefe Donsa pyroclastic deposits (CD). The position of this fault system is shown by the black box in Figure 6. The location of Figure 9d is indicated on the map. Throws are derived from LiDAR and Aster data. Slip rates are calculated based on the ages stated (Abebe, Manetti, et al., 2005; Chernet et al., 1998; Siegburg et al., 2018). The location of the relay ramps (R1 and R2) are labeled.

strain transfer. For example, the distributed network of closely spaced faults north of Bericha (Figure 6), as well as faults south of the BBVC, has small-scale linkages shown by splayed faults (e.g., between Faults III and IV and between the Bofa basalt and Gudda lavas) at the transition between different geological units (e.g., Figures 8–10). Transfer zones with antithetic dipping faults are observed between both BMS fault zones as horsts (Figures 6 and 9) and grabens on different scales (e.g., Figures 1 and 6), which form drainage basins, most notably at the segment tips. However, our focus in this section is on

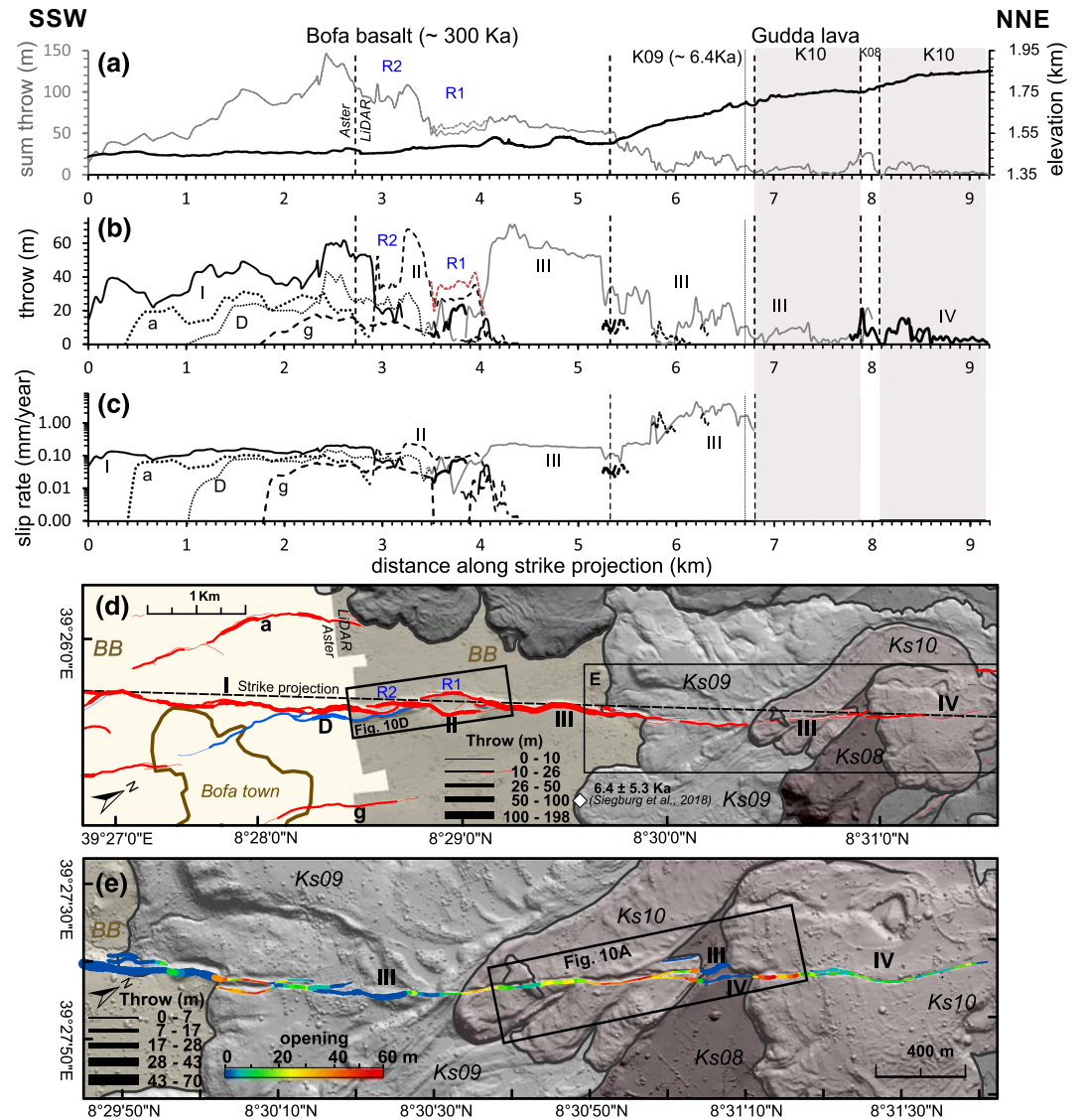


Figure 9. Analysis of a major normal fault offsetting the Bofa basalt and Gudda lavas (see Figure 8f for location). (a) Cumulative throw; (b) throw of faults in the Bofa basalt (BB) and corrected throw (adding Chefe Donsa unit on the hanging wall) at Relay Ramp 1; and (c) slip rate variation along individual faults. Throws are measured from Aster and LiDAR data while slip rates are derived from the stated ages (Chernet et al., 1998; Siegburg et al., 2018). (d) Geological map based on LiDAR and Aster data showing throw (line thickness) and dip direction to the NW (red) and SE (blue). The map is linked to throw and slip rate diagrams (a–d). (e) Detailed geological map (see d for outline) of Gudda lavas showing opening (line color) and throw (line thickness). Locations of relay ramps (R1 and R2) are labeled in map (d).

transfer-linkage zones between faults of the same dip direction in the BMS, as these play an important role for fault growth in the northern MER.

We found four relay ramps covered by LiDAR data and nine relay ramps within ASTER data at the southern central and western segment axis as well as within the distributed fault network north of Bericha (Figures 6 and S2). Those relay ramps vary in width (0.07–0.51 km), length (0.2–2.4 km), total displacement (4–130 m), and ramp displacement (<8.7 m) (Figure S2). Maximum along-ramp slopes (measured parallel to the fault scarp) are up to ~18°, ~6°, and ~28° in the lower, medium, and upper parts of the ramp, respectively (Figure S2). They tilt mostly toward the dip direction of the faults (across-ramp slope up to ~6°). Slope angles depend on length, displacement of faults, and state of breaching. We observe that larger faults have lower along-ramp slopes and that more developed breached ramps are steeper. Cross-ramp slopes correlate with

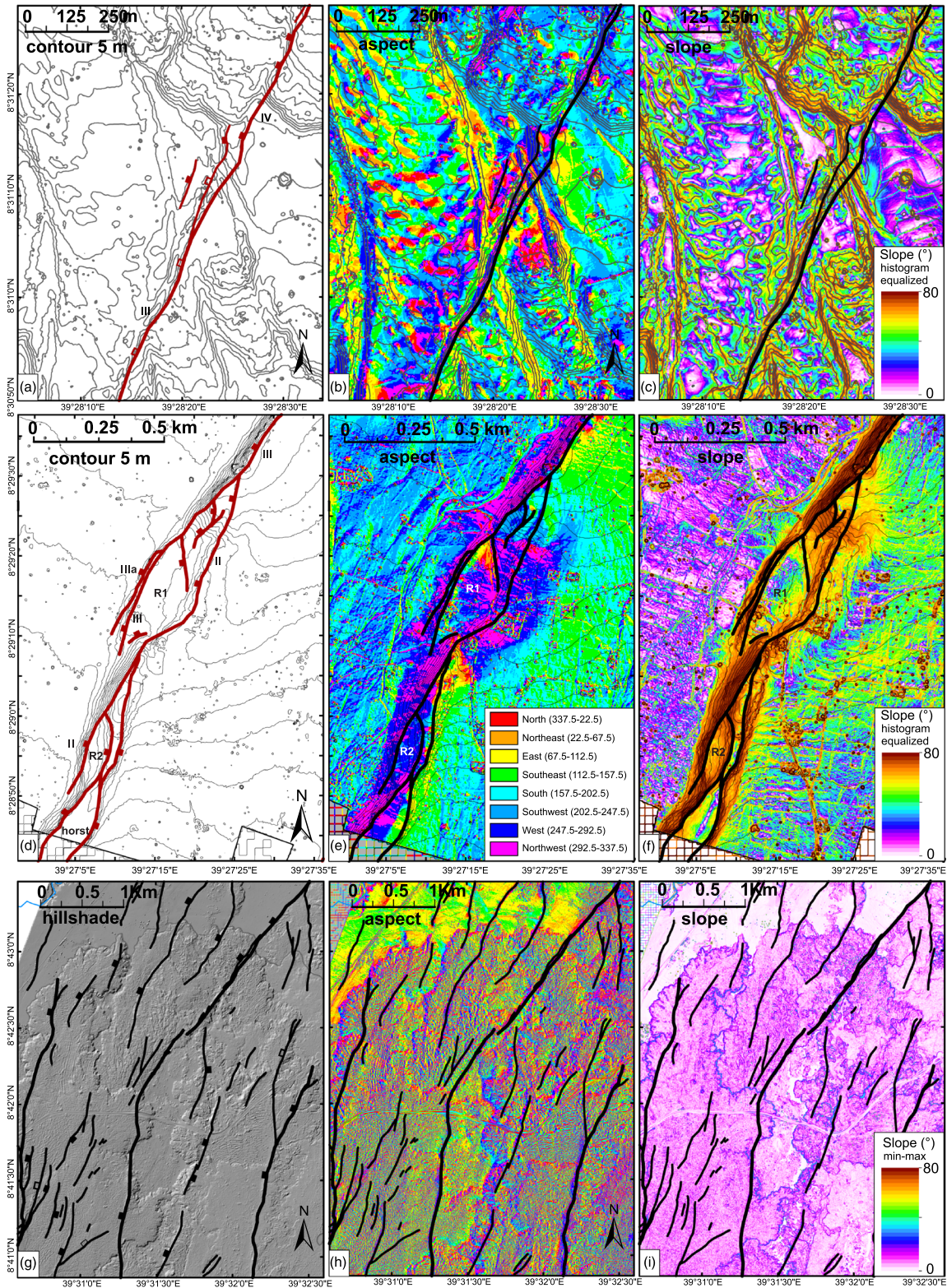


Figure 10. Fault linkage at the BMS imaged from Lidar data using 5-m contour intervals (a, d), hillshade (g), dip direction-aspect maps (b, e, and h) and slope maps (c, f, and i). (a–c) Fault splay at the transition of different lava flows of the southern slope of Gudda. (d–f) Relay Ramps R1 and R2 in the Bofa basalt south of the Gudda Volcano, (location indicated in Figure 9). Southern Relay Ramp R1 is fully breached while Northern Relay Ramp R2 is partially breached. NW dips east of Footwall II is a result of erosion of material on the footwall, which was deposited on the relay ramp R2. (g–i) Distributed faults between the central and western fault zone north of the BBVC edifice.

the displacement of the ramp. Total displacement:width and length:width ratios of relay ramps have an average value of ~ 2.8 and ~ 0.26 , respectively (Figure S2).

6.2. Linkage Characteristics and Throw Variation Along the Southern Central Axis of the BMS

A particularly well-exposed NW dipping normal fault on the central fault zone was examined in detail (box in Figure 6; Figures 8 and 9). This fault system contains three main fault parts (A0–A; B–D; and I–IV) that offset three different geological units (the Nazret unit, the Bofa basalt, and Gudda lavas) as well as several different lavas on the slope of Gudda (Figure 8). In the Nazret pyroclastic rock unit (Abebe, Manetti, et al., 2005; Boccaletti et al., 1999), the vertical fault displacement reaches ~ 90 – 130 m (Faults A0 and A) across a felsic dome and lava flows, and ~ 40 – 60 m where welded pyroclastic pumice deposits dominated (Faults A and B) (Figure 8). The Bofa basalt lava flows (300 ± 50 Ka; Chernet et al., 1998) are partially covered by thin layers of soil, pumice, ash, and river deposits of the Chefe Donsa Pyroclastic unit (40-m maximum thickness; Abebe, Manetti, et al., 2005) (Figure 8). Faults A (max throw 50 m) and B (max throw 56 m) continue from Nazret into the Bofa basalt unit and are linked by a large-scale relay ramp into Fault Systems I to IV, where Faults IB 1–3 (max throw of ~ 23 m) behave as breaching faults. Fault C (max throw of ~ 36 m) is linked by a small-scale relay ramp to Fault B. ESE dipping Fault D (max throw of ~ 43 m) is linked by a horst to NW dipping Fault I (max throw of ~ 61 m) (Figure 8). Within the southern edge of LiDAR data, WNW dipping Fault II (max throw of ~ 68 m) is linked to Fault I by a fully breached relay ramp (Figures 9 and 10; R2). Both fault tips (I and II) at the relay ramp are curving toward each other and forming a lens-shaped westward dipping relay plateau, which is integrated in the fault scarp of Fault II (Figure 10).

Fault II links by a stepwise nearly breached relay ramp (R1; Figures 8–10) to Fault III. The tips of both segments (II and III) at the ramp rotate toward the adjacent segment. The lower part of the ramp has an along ramp slope of $\sim 8^\circ$, dipping SW. The relay ramp is dipping slightly NW and has small SE dipping flexure on the northern part of ramp fault scarp III (Figure 10). Volcanic material is eroded from the footwall of Fault II and deposited on the ramp. Breaching faults between Faults II and III are oriented parallel (NNE striking) and oblique (NNW striking and WSW dipping) to both faults. Oblique breaching faults north of the ramp are well developed with maximum throws of ~ 15 m (Figure 10). North of the relay R2, Fault III continues as a normal fault through the Bofa basalt with a flexure and ESE steep back-tilting of the footwall where the largest vertical displacement of ~ 72 m occurs (Figure 10). WNW dipping Faults *a* (max throw of ~ 30 m) and *g* (max throw of ~ 17 m) are parallel to the main fault system (Figures 8 and 9).

Toward the north, Faults III and IV are characterized by opening and normal faulting through four different lava flows of Gudda (Figure 9). Opening of fractures is amplified in some parts by erosion, whereas throw measurement varies due to the rough morphology of lava (e.g., ropey-flow structures and cooling structures) as well as large lava flow thicknesses of 50–130 m. The southernmost flow unit (Ks09) contains a channel-like flow in the center (6.4 ± 5.3 Ka; Siegburg et al., 2018) and is interpreted to cover the flow Ks08. The youngest flow Ks10 has flowed from the hanging to footwall on top of the channeled flow part of Ks09 (Figure 9), suggesting a resurfacing before emplacement of lava Ks10. The large step in decreasing throw and change from normal fault to opening-normal fault in the Bofa basalt to Gudda lava flows, consistent with the lava flow thickness, suggests that Fault III became reactivated and linked to fault IV after Gudda lava flow emplacement (Figures 8 and 9). The asymmetric shape of the displacement-distance profiles of the southern fault system (Figures 9 and 10) with southward increases for Faults A, C, II, III, IV, and northward for Faults B and I indicates fault interaction and displacement transfer around linkage zones.

Fault III varies in throw between 5–20 m (Ks09) and 3–6 m in the central channel part of Ks09. In the lava Ks10, Fault III has up to 10m throw and 3 to 53m opening (Figure 9). This fault splayed within lava Ks08 into three normal faults with a maximum throw of ~ 21 m and continues as a normal-opening fault IV in the upper part of Ks10 with a maximum throw of ~ 15 -m and 9- to 33-m opening (Figure 9). The fault becomes obscured by the cone to the north, which is the source of the flow Ks10 (Figure 9).

Cumulative throw over the detailed study area averages ~ 80 m in the Nazret and the Bofa basalt unit (Figure 8a) but decreases to ~ 20 m in Gudda lavas (Figures 8a and 9a). Maximum cumulative throws are on dome structures in the Nazret unit (~ 128 m) and horst structures in the Bofa basalt (~ 149 m) (Figure 8a). Lows in cumulative throws are enhanced by erosion in Nazret pyroclastics (Figure 8) as well as at fault linkage areas (relay ramps) (e.g., Figure 10) in the Bofa basalt and where large openings occur

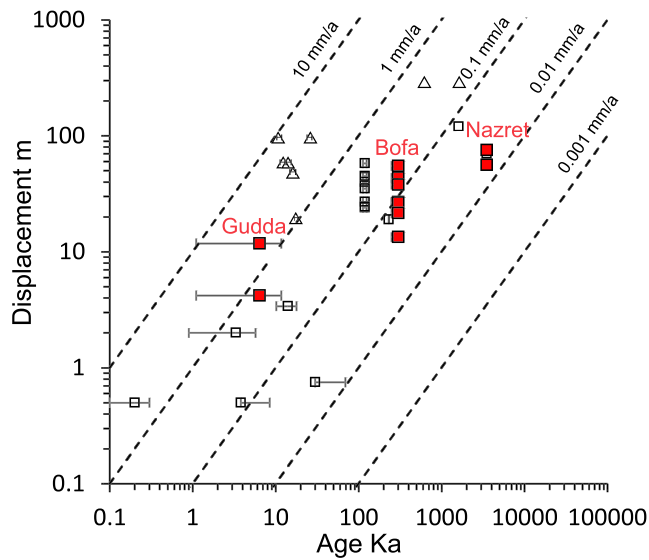


Figure 11. Normal fault displacement versus lava flow age plotted on a log-log plot. The data indicate an increasing slip rate for the BMS over time. Data at the southern fault investigated in detail in this study (red squares) in Guddas lava, Bofa basalt, and Nazret pyroclastic unit. They are supported by additional displacement data (this study) within the volcanic units around the BBVC (open squares) dated by Chernet et al. (1998), Morton et al. (1979), and Siegburg et al. (2018), also shown in Figure 6. Slip rate data from Soddo region south Ethiopia (Corti, Ranalli, et al., 2013) and Asela border fault (Abebe, Manetti, et al., 2005) in the MER are shown (open triangles).

in Gudda lavas (Figure 9). In addition to measuring fault throws, we classified the faults using throw:opening (T/O) ratios (Figure 9e; Text S1).

7. Fault Activity

Siegburg et al. (2018) determined a relative and absolute chronology of the BBVC lava flows, which, in addition to previous age constraints of the lavas (Abebe, Manetti, et al., 2005; Chernet et al., 1998; Morton et al., 1979) around the BBVC edifice, can be used to determine minimum slip rates from fault displacement data (Figures 6–9; Table S3). Slip rates of faults cutting through the rift floor around the BBVC range between 0.012 and 0.15 mm/year. However, slip rates of faults cutting through Quaternary lava flows of the BBVC are apparently higher, ranging between <0.2 and 0.53 mm/year. Faults cutting through the most recent lava flows on top of the BBVC have deep cracks with only minor or no vertical displacement (Figures 3, 6, and 10).

For our detailed fault investigation south of the BBVC (Figures 8–10; Table S3), slip rates are based on cumulative throws. In the Bofa basalt ($\sim 300 \pm 50$ Ka; Chernet et al., 1998), slip rates range up to ~ 0.24 mm/year. If the throw is adjusted to include the maximum thickness of Chefe Donsa pumice (40 m) onto the hanging wall, the slip rate range increases to ~ 0.37 mm/year (Figure 8). Slip rates of faults cutting through the Nazret unit (~ 2.5 Ma; Abebe, Manetti, et al., 2005) are up to ~ 0.05 mm/year; however, a similar vertical separation of faults in the Nazret unit and the Bofa basalt suggests

activity of this fault system started soon after the Bofa basalt was emplaced, which results in slip rates of up to ~ 0.43 mm/year (Figure 8). The slip rates in Gudda lava flows are up to ~ 4.3 mm/year in Fault III (Figure 9). In all three units, the range of slip rates, as well as the increase from the Bofa basalt to Gudda lavas, covers an order of magnitude (Figure 11).

8. Discussion

8.1. Obliquity of the Northern MER

We place quantitative constraints on rift obliquity in the northern MER of $\alpha = 31$ to 45° (Figures 4 and 12) based on the angular relation between rift trend and plate motion vector (Figures 2 and 4). Rift obliquity is highest in the north and becomes more orthogonal in the south (Figure 1). We observe a small change in the obliquity of $\sim 7^\circ$ over several magmatic segments (Figures 2 and 12), suggesting the northern MER is associated with transtensional kinematics with an increasing shear component northwards (Figures 2 and 4). The change in the shear component is hypothesized to be related to purely tectonic processes (Corti, 2008), such as preexisting cross-rift structures (e.g., YTVL: Bonini et al., 2005; Kessem River: Wolfenden et al., 2005) (Figure 1), as has also been suggested in the Kenyan rift (Robertson et al., 2015). A component of strike-slip motion may be accommodated by local variation of stress fields most likely near the tips and in the transfer zone between an echelon magmatic segments. Evidence for this is shown from rotation of crustal blocks from paleomagnetic and structural data near Fantale (Corti, Philippon, et al., 2013; Kidane et al., 2006, 2009), and the positions of left-lateral strike-slip focal mechanisms in the MER being near the segment tips (Keir et al., 2006), consistent with a left-lateral transtension component (e.g., Muluneh et al., 2014).

An alternative to the tectonic kinematic-induced change of magmatic segment and plate motion vector orientations could be along-rift variations in magmatism. If fluid pressure P_f (assuming fluid = magma) exceeds the minimum principal compressive stress σ_3 of the regional stress field, a dike intrusion can open a new or preexisting fracture (Delaney et al., 1986; Jolly & Sanderson, 1997). The direction of dike intrusion is preferably perpendicular to σ_3 ; however, if $\sigma_3 < P_f < \sigma_2$, a limited range of different fracture orientations

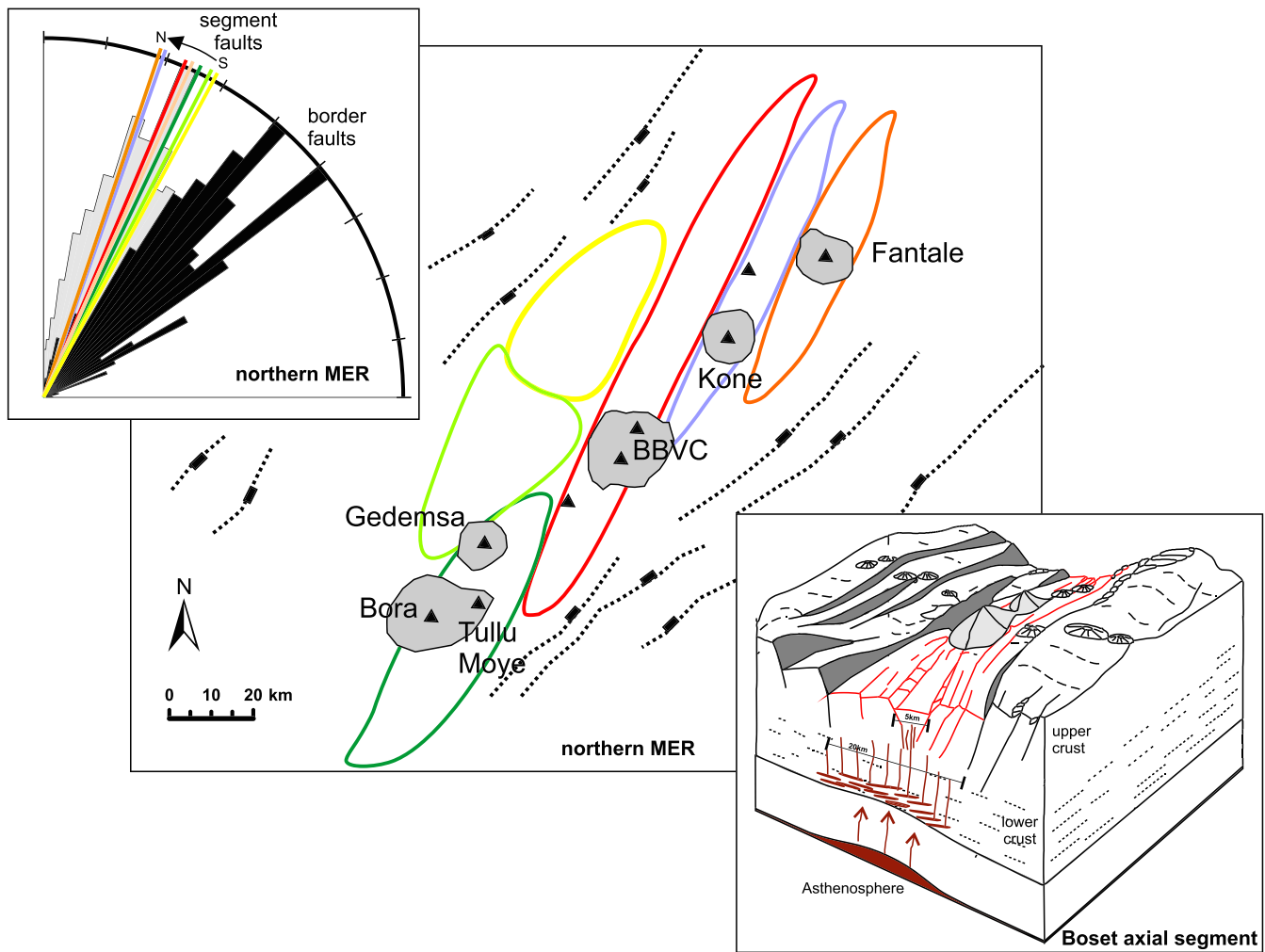


Figure 12. Summary of fault orientations within the northern MER, including border faults (black) and segment faults (gray). The length-weighted strike average of each segment (color) decreases from south to north. Colors fault segments in the rose diagram and map are linked to Figure 2. Schematic block diagram integrating our surface observations of the Boset magmatic segment with geophysical interpretations of a shallow 5-km-wide dike intrusion zone below the inner graben of the BMS and a 20-km-wide intrusion zone in the lower crust (modified after Dunn et al., 2005).

are able to open and with $P_f > \sigma_2$ fractures of any orientation can open (Jolly & Sanderson, 1997). The magmatic influence is shown by slightly more oblique aligned cones and craters at Kone and the BMS compared to fault strike averages (Table S2), as well as radial aligned cones on volcanic centers (e.g., Siegburg et al., 2018).

Our analyses of rift obliquity, when compared to analyses of spreading centers (Figure 4; Tuckwell et al., 1996) shows that this part of the MER is characteristic of that of slow spreading ridges such as the Mohn's Ridge (Dauteuil & Brun, 1993, 1996), Reykjanes Ridge (Jefferis & Voight, 1981; Tuckwell & Sanderson, 1998), and western Gulf of Aden (Dauteuil et al., 2001; Tamsett & Searle, 1988) (Figure 4). This similarity is consistent with the hypothesis that the kinematics and architecture of slow spreading ridges initiate prior to continental breakup.

8.2. The Structural Characteristic of a Magmatic Segment

The structural observations on the surface of the BMS suggest tectonic evolution on different spatial scales. The magmatic segment comprises an ~5-km-wide graben, which is bounded by NNE-SSW orientated fault cluster zones (western and central fault zones). The center of the segment comprises a zone of aligned craters and cones, fissures, and sources of most lava flows, where the BBVC represents the southern part of this magmatic zone.

A caldera with a remnant caldera rim on the western fault zone and a buried caldera rim on the central fault zone is aligned to the extent of the graben (Figures 1 and 6). Magmatism dominantly occurs along the eastern sides of the graben (central axis) at, and north of, the BBVC edifice. The distribution of magmatism and the greater number of NW dipping faults along the magmatic segment (Figure 6) indicate asymmetry within the segment with the eastern fault zone being dominant. This asymmetry is similar to the rift-scale border fault asymmetry in the northern MER with the eastern fault zone being dominant, as indicated by higher and steeper eastern border topography, more consistent border fault orientations, and tilted rift floor topography (Figures 1, 2, and 5). This is in accord with previous regional-scale studies showing that most of the rift length is asymmetric (e.g., Corti, 2009; Corti et al., 2018; Ebinger & Casey, 2001; Keir et al., 2015).

The western side of the axial graben is dominated by SE dipping normal faults (north and south of the edifice) with larger vertical displacement and higher throw:length ratios compared to the central fault zone (Figures 6 and 7). This contrasting geometric distribution suggests dominant tectonic strain on the western fault zone. Volcanic deposits covering faults coupled with the magmatic extension may explain the lower fault displacement in the central fault zone. Alternatively, the SE dipping faults could be older. The only exposed NW dipping faults occur in the young lavas on the western axis (Figure 6), suggesting a geometric change over time.

Both sides of the graben have distributed faults and fractures north of the edifices, whereas toward the segment tips the faults are more localized and have higher displacements and higher maximum throw:length ratios (Figures 6, 7, and 9), even in close proximity (southern central axis) to the edifice.

Our results show evidence for higher amounts of fault slip near the magmatic segment tips, and lower amounts of faulting at the magmatic segment center with a higher cone density (Figures 2 and 6). This observation is consistent with the hypothesis of a segment-centered focus of magmatism (Keir et al., 2009; Kurz et al., 2007).

A similar tectono-magmatic distribution on the surface and overall graben within the segment is also observed at neighboring segments, for example, Kone and Fantale segments (Figures 1 and 2), and at other rift zones such as Dabbahu in Afar (Rowland et al., 2007) and Krafla in Iceland (Opheim & Gudmundsson, 1989). The nested graben within a segment, when compared to the overall rift graben suggests multiple rifting events, may be caused by different dike width zones and intrusion depths (Trippanera et al., 2015).

8.3. Long-Term Versus Short-Term Slip Rates in an Active Rift Segment

Quaternary slip rates of individual faults around the BBVC are heterogeneous and increase a hundredfold where normal faults and fissures offset young lavas (<16 Ka) (Figures 8 and 9). To explain this pattern, we compare slip and extension rates of the BMS with other MER fault activity and overall slip rate evolution.

Our vertical slip rates of faults crossing Gudda deposits (up to ~4.3 mm/year) agree with minimum slip rates of 0.5 to 1.5 mm/year in Pleistocene to Holocene deposits at the Asela border fault (Abebe, Manetti, et al., 2005), and with maximum slip rates of 1 to 9 mm/year of the southern Ethiopian Soddo region (Corti, Ranalli, et al., 2013). Earlier studies suggest a rate of 0.3 mm/year based on a dated ignimbrite in the southern WFB (Mohr et al., 1980), agreeing with a long-term average rate over the last 3 Ma (Mohr, 1973) and from our study (using an average of all throw measurement of individual faults).

Short-time period measurements of slip rate tend to be more heterogeneous (time intervals <20 Ka) compared to longer period (time periods of >300 Ka) measurements, as the longer time period averages out periods of high and lower activity (e.g., Mouslopoulou et al., 2009). In more detail, fault interaction and linkage driven by regional strain rates would result in slip rate variation (Acocella et al., 2000; Faure Walker et al., 2009) on timescales of <30 to 40 Ka (Mouslopoulou et al., 2009; Nicol et al., 2006), whereas a change in recurrence interval and amount of slip during earthquakes provide slip rate variations on timescales of 10 to 20 Ka (Mouslopoulou et al., 2009) and may appear as an acceleration of fault slip rates in recent periods (Nicol et al., 2009). Similar cycles are also observed for magmatism in the MER (e.g., Fontijn et al., 2018; Hutchison et al., 2016) and in the BMS (Siegburg et al., 2018). We therefore expect the same temporal bias in slip rates regardless of whether the faulting is tectonically or magma driven.

Overall, there are a lack of slip rate estimates from the northern MER (Figure 11), and because of this, it is hard to interpret the significance of our range of slip rate observations on different timescales (max ~0.37 mm/year over 300 Ka; ~4.3 mm/year over 6.4 Ka) (Figures 8, 9, and 11; Table S3). The data in Figure 11 have a wide scatter and can be fitted either by a polynomial or linear trend, representing increased rates of activity more recently (Siegburg et al., 2018) or averaging out over longer timescales of periods of activity/inactivity, respectively.

8.4. Implications for Fault Growth and Linkage Models in a Magmatic Segment

Isolated normal faults are normally considered to grow by accumulating displacement while increasing their length or by maintaining a constant length (e.g., Dawers & Anders, 1995; Gudmundsson, 1992). Additionally, linking of multiple faults (e.g., relay ramps, y-shape tip, and en echelon fault) facilitates the transfer of displacement between faults and enables fault growth (e.g., Cartwright et al., 1995; Peacock, 1991; Peacock & Sanderson, 1991, 1994; Walsh & Watterson, 1988). Our study shows the importance of fault growth by linkage on different scales in the MER.

A large-scale linkage within the magmatic segment is shown by the western and central BMS fault zones linked by NNW to NE orientated large faults (Figures 6 and 10g), supporting the inward propagation of overall rift evolution (Corti et al., 2010). These linking faults represent the third and the innermost fault population (1, border faults; 2, axial fault zones; and 3, linking axial fault zones). At the central part of the segment, fault orientations can be influenced by dike or radial edifice stress fields (Figure 1). At the segment tips, young NNE orientated faults cut or propagate into old NE orientated faults (Figures 1 and 2) and result in complex rhomb-shaped, splay patterns, and curved faults, forming an overall sigmoidal segment shape (Boccaletti et al., 1999; Casey et al., 2006; Kurz et al., 2007; Mohr, 1967). This linkage with N-NE faults is also observed on a small scale between faults forming relay ramps (Figures 6, 8, and 10).

Relay geometries around the BBVC (Figure S2) have total average length:width ratios of ~3, with most of them slightly less due to the presence of rather large-scale relays. This is consistent with the relay ramp data compilation of Long and Imber (2011) and Fossen and Rotevatn (2016) (Figure S2). Compared to those studies, the middle part of the along-ramp slope of our partly to fully breached relays (up to ~6°) (e.g., Figures S2) is slightly lower than reported unbreached relay ramp slopes ($6.6^\circ \pm 3.3^\circ$), whereas the lower and upper parts of the along-ramp slope are comparable to the reported barely ($12.6^\circ \pm 4.5^\circ$) or strongly ($17.8^\circ \pm 8^\circ$) breached ramp slopes (Fossen & Rotevatn, 2016). The total displacement:width ratios of relay ramps have on a bi-log scale a trend of 0.24 ($R^2 = 0.67$). Based on the linkage criterion of Soliva and Benedicto (2004) ($d/w > 1$, fully breached; $d/w < 0.27$, open relay), only Relay Ramp R2 can be interpreted to be closest to fully breached state, three relays are considered as open relays, and all other measured relays are considered to be in the breaching phase. Differences between surface observation and relay geometry breaching indicators may suggest asymmetric branching at depth (Soliva et al., 2008).

Differences between our and previous studies can be explained by the presence of more brittle lava in the MER relative to the sandstone/limestone encountered in most other relay studies. Further, if sedimentation or volcanic clastic deposition occurs at the same time as the formation of relay ramp (e.g., Figure 9), the ramp is expected to be steeper and more mature in depth within the same geological formation compared to the surface (Giba et al., 2012).

Further linkage and growth patterns can be determined on asymmetric fault displacement-distance profiles as suggested by Manighetti et al. (2001) for the Afar region. The asymmetric shape of displacement-distance profiles of faults along the southern part of the central fault zone (Figures 8 and 9) are angled with the higher displacement away from the volcanic edifice (Faults II–IV, C, and A), as would be expected for a dike intrusion sourced by the volcanic center. However, considering those trends together with displacement-distance profiles of faults (B and I) indicates that this asymmetry is more likely to be due to kinematic interaction at linkage zones (e.g., Cartwright et al., 1995, 1996; Peacock & Sanderson, 1991) on the scale of one fault system within a segment. These fault geometry relations suggest that fault linkage plays a significant role for the tectonic activity and fault growth in the BMS, in particularly for segment tips and the western fault zone.

8.5. Contribution of Faulting to Extension

The contribution of the fault system of the central axis south of the BBVC, described in Figures 8 and 9, to the overall rift extension, is determined by comparing long- and short-term displacement analyses derived from

LiDAR/Aster data and chronological control with geodetic measurements made over a shorter timescale. We calculate extension rates with a typical normal fault dip angle of 60° at the surface (45° heave at depth = throw) (Rowland et al., 2007) for calculation of heave for individual faults (Table S3). We applied the extension rates on corrected displacement profiles, considering maximum 40m Chefe Donsa Pyroclastic deposits (Table S1; Abebe, Manetti, et al., 2005). This approach yields average extension rates (summed over the studied fault system) of 0.14 ± 0.103 mm/year (0.24 ± 0.107 mm/year) in the Bofa basalt and 0.82 ± 0.749 mm/year (1.42 ± 1.220 mm/year) in Gudda lavas (Table S3). Our results show that the extension rate calculated with a dip angle of 45° is 1.7 times higher than the extension rate calculated from a dip angle of 60° of the summed southern faults.

GPS data collected during 1995–2015 indicated ~ 2 mm/year of extension in the rift valley, of which the majority is in the magmatic segments (Birhanu et al., 2016). Assuming the same scenario over the last ~ 300 Ka, we compute that the southern part of the BBVC central fault zone accumulates only $\sim 5\%$ of the extension in the Bofa basalt (ASTER + LiDAR) and $<50\%$ of the extension in the Gudda (LiDAR) lavas. The latter value suggests that the investigated fault system contributed significantly to the overall rift extension in the last ~ 6 Ka. The remaining extension either occurs on rift valley faults not sampled in our study or via alternative modes of extension such as dike intrusion. The calculated extension rates in the ~ 300 Ka Bofa basalt are of a similar magnitude compared to extension rates reported at Fantale with 0.1 mm/year in a 168 ± 38 Ka welded tuff (Williams et al., 2004).

9. Conclusions

Detailed structural analyses of fault networks, kinematics, and activity on segments in a magma-assisted continental rift were applied to the MER and in more detail on the BMS to estimate fault activity rates, characterize the structural style of a segment, and understand the relative contribution of faulting.

Large-scale obliquity in the northern MER increases toward Afar with transtensional kinematics for individual magmatic segments (Gedemsa to Fantale).

We found that the BMS is characterized by two main NNE orientated fault zones, bounding a nested graben and a remnant caldera. Magmatism is focused on the central part of the segment along the central fault zone, indicating asymmetry in magma supply. This is consistent with rift-scale asymmetry with the dominant margin on the eastern side of the MER. Normal faults with the largest vertical displacement and displacement:length ratio are observed outside the volcanic edifice on the entire western fault zone (up to ~ 190 m) and toward the segment tips of the central fault zone (up to ~ 100 m).

Fault growth by linkage on different scales plays an important role in the evolution of the magmatic segments. Relay ramp length:width ratios are consistent with previous studies, indicating active breaching stages. Faulting dominates on the western axis and toward the segment tips by tectonic fault interaction, suggesting a significant contribution to the overall extension. Maximum slip rates are ~ 0.37 mm/year in ~ 300 Ka volcanic deposits and ~ 4.3 mm/year offsetting ~ 6 Ka old lavas. The difference in slip rates through time is likely caused by the heterogeneity of earthquake recurrence times and fault linkage, indicating short-term variation or a recent very active episode compared to long-term low average slip rates.

Data Availability Statement

The LiDAR DEM data set is published and available online (under the link <https://doi.org/10.5258/SOTON/D1347>).

References

- Abebe, B., Coltorti, M., & Pizzi, A. (2005). Rates of Late Quaternary deformation along the Wonji fault belt in the lakes region, Main Ethiopian Rift. *Rendiconti Della Societa Geologica Italiana*, *1*, 1–2.
- Abebe, T., Manetti, P., Bonini, M., Corti, G., Innocenti, F., Mazzarini, F., & Peckzay, Z. (2005). Geological map (scale 1: 200,000) of the northern Main Ethiopian Rift and its implication for the volcano-tectonic evolution of the rift. *Geological Society of America, Map and Chart Series*, MCH094.
- Accocella, V., Abebe, B., & Korme, T. (2011). Holocene opening directions along the axes of the *Red Sea (Afar) and Main Ethiopian Rifts: An overview*, *2478(02)*, 25–35. [https://doi.org/10.1130/2011.2478\(02\)](https://doi.org/10.1130/2011.2478(02))

Acknowledgments

We would like to thank the NERC Airborne Research and Survey Facility (Grant ET12-14) for undertaking a LiDAR survey over the BBVC. We thank the staff of the Institute of Geophysics, Space Science, and Astronomy and Department of Earth Science at Addis Ababa University, Ethiopia, for support during data collection (2012) and fieldwork (2015). We thank WUN for the possibility of a research visit at the University of Bergen. The constructive reviews by Cindy Ebinger and Julie Rowland are highly appreciated and led to significant improvements of the manuscript. The research is partly supported by the Italian Ministero Università e Ricerca MIUR through Grant PRIN 2017P9AT72.

- Acocella, V., Gudmundsson, A., & Funicello, R. (2000). Interaction and linkage of extension fractures and normal faults: Examples from the rift zone of Iceland. *Journal of Structural Geology*, *22*, 1233–1246. Retrieved from papers3://publication/uuid/D9D69A42-728B-4112-874E-E7925364AFBF
- Acocella, V., & Korme, T. (2002). Holocene extension direction along the Main Ethiopian Rift, East Africa. *Terra Nova*, *14*(3), 191–197. <https://doi.org/10.1046/j.1365-3121.2002.00403.x>
- Acocella, V., Korme, T., & Salvini, F. (2002). Formation of normal faults along the axial zone of the Ethiopian Rift. *Journal of Structural Geology*, *25*(4), 503–513. [https://doi.org/10.1016/S0191-8141\(02\)00047-0](https://doi.org/10.1016/S0191-8141(02)00047-0)
- Agostini, A., Bonini, M., Corti, G., Sani, F., & Manetti, P. (2011). Distribution of Quaternary deformation in the central Main Ethiopian Rift, East Africa. *Tectonics*, *30*, TC4010. <https://doi.org/10.1029/2010TC002833>
- Agostini, A., Bonini, M., Corti, G., Sani, F., & Mazzarini, F. (2011). Fault architecture in the Main Ethiopian Rift and comparison with experimental models: Implications for rift evolution and Nubia-Somalia kinematics. *Earth and Planetary Science Letters*, *301*(3–4), 479–492. <https://doi.org/10.1016/j.epsl.2010.11.024>
- Bailey, W. R., Walsh, J. J., & Manzocchi, T. (2005). Fault populations, strain distribution and basement fault reactivation in the East Pennines Coalfield, UK. *Journal of Structural Geology*, *27*(5), 913–928. <https://doi.org/10.1016/j.jsg.2004.10.014>
- Bendick, R., McClusky, S., Bilham, R., Asfaw, L., & Klemperer, S. (2006). Distributed Nubia-Somalia relative motion and dike intrusion in the Main Ethiopian Rift. *Geophysical Journal International*, *165*(1), 303–310. <https://doi.org/10.1111/j.1365-246X.2006.02904.x>
- Bilham, R., Bendick, R., Larson, K., Mohr, P., Braun, J., Tesfaye, S., & Asfaw, L. (1999). Secular and tidal strain across the Main Ethiopian rift. *Geophysical Research Letters*, *26*(18), 2789. <https://doi.org/10.1029/1998GL005315>
- Birhanu, Y., Bendick, R., Fisseha, S., Lewi, E., Floyd, M. A., King, R., & Reilinger, R. (2016). GPS constraints on broad scale extension in the Ethiopian Highlands and Main Ethiopian Rift. *Geophysical Research Letters*, *43*, 6844–6851. <https://doi.org/10.1002/2016GL069890>
- Boccaletti, M., Mazzuoli, R., Bonini, M., Trua, T., & Abebe, B. (1999). Plio-Quaternary volcanotectonic activity in the northern sector of the Main Ethiopian Rift: Relationships with oblique rifting. *Journal of African Earth Sciences*, *29*(4), 679–698. [https://doi.org/10.1016/S0899-5362\(99\)00124-4](https://doi.org/10.1016/S0899-5362(99)00124-4)
- Bonini, M., Corti, G., Innocenti, F., Manetti, P., Mazzarini, F., Abebe, T., & Pecskey, Z. (2005). Evolution of the Main Ethiopian Rift in the frame of Afar and Kenya rifts propagation. *Tectonics*, *24*, TC1007. <https://doi.org/10.1029/2004TC001680>
- Bubeck, A., Walker, R. J., Imber, J., & MacLeod, C. J. (2018). Normal fault growth in layered basaltic rocks: The role of strain rate in fault evolution. *Journal of Structural Geology*, *115*(July), 103–120. <https://doi.org/10.1016/j.jsg.2018.07.017>
- Bull, J. M., Minshull, T. A., Mitchell, N. C., Thors, K., Dix, J. K., & Best, A. I. (2003). Fault and magmatic interaction within Iceland's western rift over the last 9 kyr. *Geophysical Journal International*, *154*(1), F1–F8. <https://doi.org/10.1046/j.1365-246x.2003.01990.x>
- Cartwright, J. A., Mansfield, C., & Trudgill, B. (1996). The growth of normal faults by segment linkage. *Geological Society Special Publication*, *99*(99), 163–177. <https://doi.org/10.1144/GSL.SP.1996.099.01.13>
- Cartwright, J. A., Trudgill, B. D., & Mansfield, C. S. (1995). Fault growth by segment linkage: An explanation for scatter in maximum displacement and trace length data from the Canyonlands Grabens of SE Utah. *Journal of Structural Geology*, *17*(9), 1319–1326. [https://doi.org/10.1016/0191-8141\(95\)00033-A](https://doi.org/10.1016/0191-8141(95)00033-A)
- Casey, M., Ebinger, C., Keir, D., Gloaguen, R., & Mohamed, F. (2006). Strain accommodation in transitional rifts: Extension by magma intrusion and faulting in Ethiopian rift magmatic segments. *Geological Society, London, Special Publications*, *259*(2003), 143–163. <https://doi.org/10.1144/GSL.SP.2006.259.01.13>
- Chernet, T., Hart, W. K., Aronson, J. L., & Walter, R. C. (1998). New age constraints on the timing of volcanism and tectonism in the northern Main Ethiopian Rift-southern Afar transition zone (Ethiopia). *Journal of Volcanology and Geothermal Research*, *80*(3–4), 267–280. [https://doi.org/10.1016/S0377-0273\(97\)00035-8](https://doi.org/10.1016/S0377-0273(97)00035-8)
- Chu, D., & Gordon, R. G. (1999). Evidence for motion between Nubia and Somalia along the Southwest Indian ridge. *Nature*, *398*(6722), 64–67. <https://doi.org/10.1038/18014>
- Cole, J. W. (1969). The Gariboldi volcanic complex. *Bulletin of Volcanology*, *33*(2), 566–578. <https://doi.org/10.1007/BF02596525>
- Cornwell, D. G., Mackenzie, G. D., England, R. W., Maguire, P. K. H., Asfaw, L., & Oluma, B. (2006). Northern Main Ethiopian Rift crustal structure from new high-precision gravity data. In G. Yirgu, C. Ebinger, & P. K. H. Maguire (Eds.), *The Afar Volcanic Province within the East African Rift System* (Vol. 259, pp. 307–321). London: Geological Society.
- Corti, G. (2008). Control of rift obliquity on the evolution and segmentation of the main Ethiopian rift. *Nature Geoscience*, *1*(4), 258–262. <https://doi.org/10.1038/ngeo160>
- Corti, G. (2009). Continental rift evolution: From rift initiation to incipient break-up in the Main Ethiopian Rift, East Africa. *Earth-Science Reviews*, *96*(1–2), 1–53. <https://doi.org/10.1016/j.earscirev.2009.06.005>
- Corti, G., Molin, P., Sembroni, A., Bastow, I. D., & Keir, D. (2018). Control of pre-rift lithospheric structure on the architecture and evolution of continental rifts: Insights from the Main Ethiopian Rift, East Africa. *Tectonics*, *37*, 477–496. <https://doi.org/10.1002/2017TC004799>
- Corti, G., Philippon, M., Sani, F., Keir, D., & Kidane, T. (2013). Re-orientation of the extension direction and pure extensional faulting at oblique rift margins: Comparison between the Main Ethiopian Rift and laboratory experiments. *Terra Nova*, *25*(5), 396–404. <https://doi.org/10.1111/ter.12049>
- Corti, G., Ranalli, G., Agostini, A., & Sokoutis, D. (2013). Inward migration of faulting during continental rifting: Effects of pre-existing lithospheric structure and extension rate. *Tectonophysics*, *594*, 137–148. <https://doi.org/10.1016/j.tecto.2013.03.028>
- Corti, G., Ranalli, G., Mulugeta, G., Agostini, A., Sani, F., & Zugu, A. (2010). Control of the rheological structure of the lithosphere on the inward migration of tectonic activity during continental rifting. *Tectonophysics*, *490*(3–4), 165–172. <https://doi.org/10.1016/j.tecto.2010.05.004>
- Corti, G., Sani, F., Philippon, M., Sokoutis, D., Willingshofer, E., & Molin, P. (2013). Quaternary volcano-tectonic activity in the Soddo region, western margin of the Southern Main Ethiopian Rift. *Tectonics*, *32*, 861–879. <https://doi.org/10.1002/tect.20052>
- Dauteuil, O., & Brun, J. P. (1993). Oblique rifting in a slow-spreading ridge. *Nature*, *361*(6408), 145–148. <https://doi.org/10.1038/361145a0>
- Dauteuil, O., & Brun, J. P. (1996). Deformation partitioning in a slow spreading ridge undergoing oblique extension: Mohns Ridge, Norwegian Sea. *Tectonics*, *15*(4), 870–884. <https://doi.org/10.1029/95TC03682>
- Dauteuil, O., Huchon, P., Quemeneur, F., & Souriot, T. (2001). Propagation of an oblique spreading centre: The western Gulf of Aden. *Tectonophysics*, *332*(4), 423–442. [https://doi.org/10.1016/S0040-1951\(00\)00295-X](https://doi.org/10.1016/S0040-1951(00)00295-X)
- Dawers, N. H., & Anders, M. (1995). Displacement-length scaling and fault linkage. *Journal of Stratigraphy*, *17*(5), 607–614.
- Delaney, P. T., Pollard, D. D., Ziony, J. I., & McKee, E. H. (1986). Field relations between dikes and joints: Emplacement processes and paleostress analysis. *Journal of Geophysical Research*, *91*(B5), 4920–4938. <https://doi.org/10.1029/JB091ib05p04920>

- DeMets, C., & Merkouriev, S. (2016). High-resolution estimates of Nubia-Somalia plate motion since 20 Ma from reconstructions of the Southwest Indian Ridge, Red Sea and Gulf of Aden. *Geophysical Journal International*, 207(1), 317–332. <https://doi.org/10.1093/gji/ggw276>
- Dunn, R. A., Lekić, V., Detrick, R. S., & Toomey, D. R. (2005). Three-dimensional seismic structure of the Mid-Atlantic Ridge (35°N): Evidence for focused melt supply and lower crustal dike injection. *Journal of Geophysical Research*, 110, B09101. <https://doi.org/10.1029/2004JB003473>
- Ebinger, C. J., & Casey, M. (2001). Continental breakup in magmatic provinces: An Ethiopian example. *Geology*, 29(6), 527–530. [https://doi.org/10.1130/0091-7613\(2001\)029<0527:CBIMPA>2.0.CO;2](https://doi.org/10.1130/0091-7613(2001)029<0527:CBIMPA>2.0.CO;2)
- Ebinger, C. J., Keir, D., Bastow, I. D., Whaler, K., Hammond, J. O. S., Ayele, A., et al. (2017). Crustal structure of active deformation zones in Africa: Implications for global crustal processes. *Tectonics*, 36, 3298–3332. <https://doi.org/10.1002/2017TC004526>
- Faure Walker, J. P., Roberts, G. P., Cowie, P. A., Papanikolaou, I. D., Sammonds, P. R., Michetti, A. M., & Phillips, R. J. (2009). Horizontal strain-rates and throw-rates across breached relay zones, central Italy: Implications for the preservation of throw deficits at points of normal fault linkage. *Journal of Structural Geology*, 31(10), 1145–1160. <https://doi.org/10.1016/j.jsg.2009.06.011>
- Fontijn, K., McNamara, K., Zafu Tadesse, A., Pyle, D. M., Dessalegn, F., Hutchison, W., et al. (2018). Contrasting styles of post-caldera volcanism along the Main Ethiopian Rift: Implications for contemporary volcanic hazards. *Journal of Volcanology and Geothermal Research*, 356, 90–113. <https://doi.org/10.1016/j.jvolgeores.2018.02.001>
- Fossen, H., & Rotevatn, A. (2016). Fault linkage and relay structures in extensional settings—A review. *Earth-Science Reviews*, 154, 14–28. <https://doi.org/10.1016/j.earscirev.2015.11.014>
- Giba, M., Walsh, J. J., & Nicol, A. (2012). Segmentation and growth of an obliquely reactivated normal fault. *Journal of Structural Geology*, 39, 253–267. <https://doi.org/10.1016/j.jsg.2012.01.004>
- Grant, J. V., & Kattenhorn, S. A. (2004). Evolution of vertical faults at an extensional plate boundary, southwest Iceland. *Journal of Structural Geology*, 26(3), 537–557. <https://doi.org/10.1016/j.jsg.2003.07.003>
- Gudmundsson, A. (1992). Formation and growth of normal faults at the divergent plate boundary in Iceland. *Terra Nova*, 4, 464–471.
- Hayward, N. J., & Ebinger, C. J. (1996). Variations in the along-axis segmentation of the Afar Rift system. *Tectonics*, 15(2), 244. <https://doi.org/10.1029/95TC02292>
- Holland, M., Urai, J. L., & Martel, S. (2006). The internal structure of fault zones in basaltic sequences. *Earth and Planetary Science Letters*, 248(1–2), 301–315. <https://doi.org/10.1016/j.epsl.2006.05.035>
- Hutchison, W., Fusillo, R., Pyle, D. M., Mather, T. A., Blundy, J. D., Biggs, J., et al. (2016). A pulse of mid-Pleistocene rift volcanism in Ethiopia at the dawn of modern humans. *Nature Communications*, 7(1), 1–12. <https://doi.org/10.1038/ncomms13192>
- Jefferis, R. G., & Voight, B. (1981). Fracture analyses near the mid-ocean plate boundary, Reykjavik-Hvalfjörður area, Iceland. *Tectonophysics*, 76, 171–236.
- Jestin, F., Huchon, P., & Gaulier, J. M. (1994). The Somalia plate and the East African Rift System: Present-day kinematics. *Geophysical Journal International*, 116, 637–654.
- Jolly, R. J. H., & Sanderson, D. J. (1997). A Mohr circle construction for the opening of a pre-existing fracture. *Journal of Structural Geology*, 19(6), 887–892. [https://doi.org/10.1016/S0191-8141\(97\)00014-X](https://doi.org/10.1016/S0191-8141(97)00014-X)
- Kaven, J. O., & Martel, S. J. (2007). Growth of surface-breaching normal faults as a three-dimensional fracturing process. *Journal of Structural Geology*, 29(9), 1463–1476. <https://doi.org/10.1016/j.jsg.2007.05.007>
- Keir, D., Bastow, I. D., Corti, G., Mazzarini, F., & Rooney, T. O. (2015). The origin of along-rift variations in faulting and magmatism in the Ethiopian Rift. *Tectonics*, 34, 1–14. <https://doi.org/10.1002/2014TC003698>. Received
- Keir, D., Bastow, I. D., Whaler, K. a., Daly, E., Cornwell, D. G., & Hautot, S. (2009). Lower crustal earthquakes near the Ethiopian rift induced by magmatic processes. *Geochemistry, Geophysics, Geosystems*, 10, QOAB02. <https://doi.org/10.1029/2009GC002382>
- Keir, D., Ebinger, C. J., Stuart, G. W., Daly, E., & Ayele, A. (2006). Strain accommodation by magmatism and faulting as rifting proceeds to breakup: Seismicity of the northern Ethiopian rift. *Journal of Geophysical Research*, 111, B05314. <https://doi.org/10.1029/2005JB003748>
- Kidane, T., Otofujii, Y. I., Komatsu, Y., Shibasaki, H., & Rowland, J. V. (2009). Paleomagnetism of the Fentale-magmatic segment, main Ethiopian Rift: New evidence for counterclockwise block rotation linked to transtensional deformation. *Physics of the Earth and Planetary Interiors*, 176(1–2), 109–123. <https://doi.org/10.1016/j.pepi.2009.04.006>
- Kidane, T., Platzman, E., Ebinger, C., Abebe, B., & Rochette, P. (2006). Palaeomagnetic constraints on continental break-up processes: Observations from the Main Ethiopian Rift. *Geological Society, London, Special Publications*, 259(1), 165–183. <https://doi.org/10.1144/gsl.sp.2006.259.01.14>
- Kurz, T., Gloaguen, R., Ebinger, C., Casey, M., & Abebe, B. (2007). Deformation distribution and type in the Main Ethiopian Rift (MER): A remote sensing study. *Journal of African Earth Sciences*, 48(2–3), 100–114. <https://doi.org/10.1016/j.jafrearsci.2006.10.008>
- Long, J. J., & Imber, J. (2011). Geological controls on fault relay zone scaling. *Journal of Structural Geology*, 33(12), 1790–1800. <https://doi.org/10.1016/j.jsg.2011.09.011>
- Mackenzie, G. D., Thybo, H., & Maguire, P. K. H. (2005). Crustal velocity structure across the Main Ethiopian Rift: Results from two-dimensional wide-angle seismic modelling. *Geophysical Journal International*, 162(3), 994–1006. <https://doi.org/10.1111/j.1365-246X.2005.02710.x>
- Manighetti, I., King, G. C. P., Gaudemer, Y., Scholz, C. H., & Doubre, C. (2001). Slip accumulation and lateral propagation of active normal faults in Afar. *Journal of Geophysical Research*, 106(B7), 13,667–13,696.
- Martel, S. J., & Langley, J. S. (2006). Propagation of normal faults to the surface in basalt, Koaie fault system, Hawaii. *Journal of Structural Geology*, 28(12), 2123–2143. <https://doi.org/10.1016/j.jsg.2005.12.004>
- McCoss, A. M. (1986). Simple constructions for deformation in transpression/transension zones. *Journal of Structural Geology*, 8(6), 715–718. [https://doi.org/10.1016/0191-8141\(86\)90077-5](https://doi.org/10.1016/0191-8141(86)90077-5)
- Mohr, P. A. (1962). Surface cauldron subsidence with associated faulting and fissure basalt eruptions at Gariboldi pass, Shoa, Ethiopia. *Bulletin Volcanologique*, 24(1), 421–428. <https://doi.org/10.1007/BF02599358>
- Mohr, P. A. (1967). Major volcano-tectonic lineament in the Ethiopian Rift System. *Nature*, 664–665. <https://doi.org/10.1038/213664a0>
- Mohr, P. A. (1973). Crustal deformation rate and evolution of the Ethiopian Rift. In D. H. Tarling, & S. K. Runcorn (Eds.), *Implications of continental drift to earth sciences* (pp. 767–776). London: Academic Press.
- Mohr, P. A., Mitchell, J. G., & Reynolds, R. G. H. (1980). Quaternary volcanism and faulting at O'A caldera, central Ethiopian rift. *Bulletin Volcanologique*, 43(1), 173–189. <https://doi.org/10.1007/BF02597619>
- Morton, W. H., Rex, D. C., Mitchell, J. G., & Mohr, P. (1979). Riftward younging of volcanic units in the Addis Ababa region, Ethiopian rift valley. *Nature*, 280(5720), 284–288. <https://doi.org/10.1038/280284a0>

- Mouslopoulou, V., Walsh, J. J., & Nicol, A. (2009). Fault displacement rates on a range of timescales. *Earth and Planetary Science Letters*, 278(3–4), 186–197. <https://doi.org/10.1016/j.epsl.2008.11.031>
- Muluneh, A. A., Cuffaro, M., & Doglioni, C. (2014). Left-lateral transtension along the Ethiopian rift and constrains on the mantle-reference plate motions. *Tectonophysics*, 632(C), 21–31. <https://doi.org/10.1016/j.tecto.2014.05.036>
- Muluneh, A. A., Kidane, T., Corti, G., & Keir, D. (2018). Constraints on fault and crustal strength of the Main Ethiopian Rift from formal inversion of earthquake focal mechanism data. *Tectonophysics*, 731–732(March), 172–180. <https://doi.org/10.1016/j.tecto.2018.03.010>
- Nicol, A., Walsh, J., Berryman, K., & Villamor, P. (2006). Interdependence of fault displacement rates and paleoearthquakes in an active rift. *Geology*, 34(10), 865–868. <https://doi.org/10.1130/G22335.1>
- Nicol, A., Walsh, J., Mouslopoulou, V., & Villamor, P. (2009). Earthquake histories and holocene acceleration of fault displacement rates. *Geology*, 37(10), 911–914. <https://doi.org/10.1130/G25765A.1>
- Opheim, J. A., & Gudmundsson, A. (1989). Formation and geometry of fractures, and related volcanism, of the Krafla fissure swarm, northeast Iceland. *Geological Society of America Bulletin*, 101(12), 1608–1622. [https://doi.org/10.1130/0016-7606\(1989\)101<1608:FAGOFA>2.3.CO;2](https://doi.org/10.1130/0016-7606(1989)101<1608:FAGOFA>2.3.CO;2)
- Peacock, D. C. P. (1991). Displacements and segment linkage in strike-slip fault zones. *Journal of Structural Geology*, 13(9), 1025–1035. [https://doi.org/10.1016/0191-8141\(91\)90054-M](https://doi.org/10.1016/0191-8141(91)90054-M)
- Peacock, D. C. P., & Sanderson, D. J. (1991). Displacements, segment linkage and relay ramps in normal fault zones. *Journal of Structural Geology*, 13(6), 721–733. [https://doi.org/10.1016/0191-8141\(91\)90033-F](https://doi.org/10.1016/0191-8141(91)90033-F)
- Peacock, D. C. P., & Sanderson, D. J. (1994). Geometry and development of relay ramps in normal fault systems. *American Association of Petroleum Geologists Bulletin*, 78(2), 147–165. <https://doi.org/10.1306/bdff9046-1718-11d7-8645000102c1865d>
- Pizzi, A., Coltorti, M., Abebe, B., Disperati, L., Sacci, G., & Salvini, R. (2006). The Wonji Fault Belt (Main Ethiopian Rift): Structural and geomorphological constraints and GPS monitoring. In G. Yirgu, C. J. Ebinger, & P. K. Maguire (Eds.), *The Afar Volcanic Province within the East African Rift System, Special Publications* (259th ed. pp. 191–207). London: Geological Society, London.
- Putz-Perrier, M. W., & Sanderson, D. J. (2008a). Spatial distribution of brittle strain in layered sequences. *Journal of Structural Geology*, 30(1), 50–64. <https://doi.org/10.1016/j.jsg.2007.10.005>
- Putz-Perrier, M. W., & Sanderson, D. J. (2008b). The distribution of faults and fractures and their importance in accommodating extensional strain at Kimmeridge Bay, Dorset, UK. *Geological Society, London, Special Publications*, 299(1), 97–111. <https://doi.org/10.1144/sp299.6>
- Robertson, E. A. M., Vye-Brown, C., Cashman, K. V., Floyd, M. A., & Biggs, J. (2015). Influence of regional tectonics and pre-existing structures on the formation of elliptical calderas in the Kenyan Rift. *Geological Society, London, Special Publications*, 420(1), 43–67. <https://doi.org/10.1144/sp420.12>
- Rooney, T. O., Bastow, I. D., Keir, D., Mazzarini, F., Movsesian, E., Grosfils, E. B., et al. (2014). The protracted development of focused magmatic intrusion during continental rifting. *Tectonics*, 33, 875–897. <https://doi.org/10.1002/2013TC003514>
- Rowland, J. V., Baker, E., Ebinger, C. J., Keir, D., Kidane, T., Biggs, J., et al. (2007). Fault growth at a nascent slow-spreading ridge: 2005 Dabbahu rifting episode, Afar. *Geophysical Journal International*, 171(3), 1226–1246. <https://doi.org/10.1111/j.1365-246x.2007.03584.x>
- Rowland, J. V., & Sibson, R. H. (2001). Extensional fault kinematics within the Taupo Volcanic Zone, New Zealand: Soft-linked segmentation of a continental rift system. *New Zealand Journal of Geology and Geophysics*, 44(2), 271–283. <https://doi.org/10.1080/00288306.2001.9514938>
- Rowland, J. V., & Sibson, R. H. (2004). Structural controls on hydrothermal flow in a segmented rift system, Taupo Volcanic Zone, New Zealand. *Geofluids*, 4(4), 259–283. <https://doi.org/10.1111/j.1468-8123.2004.00091.x>
- Rowland, J. V., Wilson, C. J. N., & Gravley, D. M. (2010). Spatial and temporal variations in magma-assisted rifting, Taupo Volcanic Zone, New Zealand. *Journal of Volcanology and Geothermal Research*, 190(1–2), 89–108. <https://doi.org/10.1016/j.jvolgeores.2009.05.004>
- Sanderson, D. J., & Marchini, W. R. (1984). Transpression. *Journal of Structural Geology*, 6(5), 449–458. [https://doi.org/10.1016/0191-8141\(84\)90058-0](https://doi.org/10.1016/0191-8141(84)90058-0)
- Siegburg, M., Gernon, T. M., Bull, J. M., Keir, D., Barfod, D. N., Taylor, R. N., et al. (2018). Geological evolution of the Boset-Bericha Volcanic Complex, Main Ethiopian Rift: 40 Ar/39 Ar evidence for episodic Pleistocene to Holocene volcanism. *Journal of Volcanology and Geothermal Research*, 351, 115–133. <https://doi.org/10.1016/j.jvolgeores.2017.12.014>
- Soliva, R., & Benedicto, A. (2004). A linkage criterion for segmented normal faults. *Journal of Structural Geology*, 26(12), 2251–2267. <https://doi.org/10.1016/j.jsg.2004.06.008>
- Soliva, R., Benedicto, A., Schultz, R. a., Maerten, L., & Micarelli, L. (2008). Displacement and interaction of normal fault segments branched at depth: Implications for fault growth and potential earthquake rupture size. *Journal of Structural Geology*, 30(10), 1288–1299. <https://doi.org/10.1016/j.jsg.2008.07.005>
- Tamsett, D., & Searle, R. C. (1988). Structure and development of the midocean ridge plate boundary in the Gulf of Aden: Evidence from GLORIA side scan sonar. *Journal of Geophysical Research*, 93(B4), 3157–3178. <https://doi.org/10.1029/JB093iB04p03157>
- Tentler, T. (2005). Propagation of brittle failure triggered by magma in Iceland. *Tectonophysics*, 406(1–2), 17–38. <https://doi.org/10.1016/j.tecto.2005.05.016>
- Tripanera, D., Ruch, J., Acocella, V., & Rivalta, E. (2015). Experiments of dike-induced deformation: Insights on the long-term evolution of divergent plate boundaries. *Journal of Geophysical Research: Solid Earth*, 120, 6913–6942. <https://doi.org/10.1002/2014JB011850>
- Tuckwell, G. W., Bull, J. M., & Sanderson, D. J. (1996). Models of fracture orientation at oblique spreading centres. *Journal of the Geological Society*, 153(1), 185–189. <https://doi.org/10.1144/gsjgs.153.2.0185>
- Tuckwell, G. W., & Sanderson, D. J. (1998). Numerical models of faulting at oblique spreading centers. *Journal of Geodynamics*, 103(B7), 15,473–15,482.
- Villemin, T., & Bergerat, F. (2013). From surface fault traces to a fault growth model: The Vogar Fissure Swarm of the Reykjanes Peninsula, Southwest Iceland. *Journal of Structural Geology*, 51, 38–51. <https://doi.org/10.1016/j.jsg.2013.03.010>
- Wadge, G., Biggs, J., Lloyd, R., & Kendall, J.-M. (2016). Historical volcanism and the state of stress in the East African Rift System. *Frontiers in Earth Science*, 4(September). <https://doi.org/10.3389/feart.2016.00086>
- Walsh, J. J., & Watterson, J. (1988). WalshWatterson1988.pdf. *Analysis of the Relationship between Displacements and Dimensions of Faults*, 10, 239–247.
- Whaler, K. A., & Hautot, S. (2006). The electrical resistivity structure of the crust beneath the northern Main Ethiopian Rift. In G. Yirgu, C. J. Ebinger, & P. K. H. Maguire (Eds.), *The Afar Volcanic Province within the East African Rift System, Special Publications* (259th ed., Vol. 259, pp. 293–305). London: Geological Society, London. <https://doi.org/10.1144/GSL.SP.2006.259.01.22>
- Williams, F. M., Williams, M. A. J., & Aumento, F. (2004). Tensional fissures and crustal extension rates in the northern part of the Main Ethiopian Rift. *Journal of African Earth Sciences*, 38(2), 183–197. <https://doi.org/10.1016/j.jafrearsci.2003.10.007>

- WoldeGabriel, G., Aronson, J. L., & Walter, R. C. (1990). Geochronology and rift basin development in the central sector of the Main Ethiopian Rift. *Geological Society of America Bulletin*, *102*(August 2009), 439–485. [https://doi.org/10.1130/0016-7606\(1990\)102<0439](https://doi.org/10.1130/0016-7606(1990)102<0439)
- Wolfenden, E., Ebinger, C. J., Yirgu, G., Deino, A., & Ayalew, D. (2004). Evolution of the northern Main Ethiopian Rift: Birth of a triple junction. *Earth and Planetary Science Letters*, *224*(1–2), 213–228. <https://doi.org/10.1016/j.epsl.2004.04.022>
- Wolfenden, E., Ebinger, C. J., Yirgu, G., Renne, P. R., & Kelley, S. P. (2005). Evolution of a volcanic rifted margin: Southern Red Sea, Ethiopia. *Bulletin of the Geological Society of America*, *117*(7–8), 846–864. <https://doi.org/10.1130/B25516.1>
- Wormald, S. C., Wright, I. C., Bull, J. M., Lamarche, G., & Sanderson, D. J. (2012). Morphometric analysis of the submarine arc volcano Monowai (Tofua-Kermadec Arc) to decipher tectono-magmatic interactions. *Journal of Volcanology and Geothermal Research*, *239–240*, 69–82. <https://doi.org/10.1016/j.jvolgeores.2012.06.004>